
Unterschrift E. Widmann



TECHNISCHE
UNIVERSITÄT
WIEN
Vienna | Austria

DIPLOMARBEIT

Development of a cryogenic Caesium Iodide detector for gravitational measurements on antihydrogen

ausgeführt an der

Fakultät der Physik
der Technischen Universität Wien

in Zusammenarbeit mit dem

Stefan Meyer Institut für Subatomare Physik
der österreichischen Akademie der Wissenschaften

unter Anleitung von

Hon.-Prof. Dipl.-Phys. Dr. Eberhard Widmann
und
Priv.-Doz. Dr. Johann Zmeskal

durch

Sebastian Kalista, BSc
Merbotogasse 45, 2700 Wiener Neustadt

September 10, 2017

Datum

Unterschrift S. Kalista

Abstract

The AEGIS Collaboration at CERN intends to perform the world's first direct measurement of the Earth's gravitational acceleration on antimatter, by sending an antihydrogen beam through a classical Moiré deflectometer. The main goal is to test the principle of the universality of free fall (Weak Equivalence Principle WEP) for antimatter, which has never been done before.

This work presents a potential detector for a first measurement of the gravitational effects on an antimatter system. The detector consists of pure Caesium Iodide crystals (CsI) and commercially available Silicon Photomultipliers (SiPM) to measure the particles produced in the corresponding annihilation processes. The CsI crystals decay times and spectra were characterized using a radioactive ^{22}Na source at room and at low temperatures. Furthermore the behaviour of the SiPMs at low temperatures was examined. The best connection at low temperatures between the scintillator and a SiPM was found in optical glue. The final combined system of CsI and SiPM was tested in a measurement at the GRACE Line at CERN using a beam of antiprotons.

Zusammenfassung

Die AEGIS Kollaboration am CERN beabsichtigt die erste direkte Messung der Erdbeschleunigung von Antimaterie durchführen. Dies wird ermöglicht, indem man einen Antihydrogenstrahl durch ein klassisches Moiré Deflektometer sendet. Das Hauptziel ist es, das schwache Äquivalenzprinzip für Antimaterie zu überprüfen.

Diese Arbeit wird einen Detektor für diese erste Messung der Gravitationseffekte an einem Antimateriesystem vorstellen. Der Detektor besteht aus reinen Cäsiumiodidkristallen (CsI) und kommerziell erhältlichen Silizium-Photomultiplier (SiPM) um die produzierten Teilchen aus den dazugehörigen Annihilationsprozessen zu messen. Die Zerfallszeiten und Spektren des CsI wurden mit Hilfe einer radioaktiven ^{22}Na -Quelle bei Raum- und tiefen Temperaturen charakterisiert. Des Weiteren wurde das Verhalten der SiPMs bei tiefen Temperaturen untersucht. Als beste Verbindung bei tiefen Temperaturen zwischen dem Szintillator und einem SiPM wurde optischer Kleber ausgemacht. Das finale zusammengefügte System aus CsI und SiPM wurde in einer Messung mit Antiprotonen der GRACE Line am CERN getestet.

Acknowledgements

Zuallererst möchte ich mich bei meinem Betreuer, Johann Zmeskal, bedanken. Seine einleitenden Worte zu AEGIS haben mich sofort für das Experiment begeistert und mir meine Entscheidung, eine Diplomarbeit am Stefan Meyer Institut zu schreiben, leicht gemacht. Durch seine Unterstützung, seine geduldige Betreuung und sein umfangreiches Wissen im Bereich der Detektorphysik hat er eine fruchtbringende Zusammenarbeit ermöglicht, wofür ich mich im Speziellen bedanken möchte. Seine Hingabe und Begeisterung für die Physik haben meinen Aufenthalt am Institut zu einer spannenden Erfahrung gemacht. Des Weiteren möchte ich mich bei Eberhard Widmann bedanken. Durch die Finanzierung meines Aufenthalts in der Schweiz wurde es mir ermöglicht unvergessliche Einblicke in das weltweit größte Forschungsinstitut zu gewinnen und dabei selbst bei einem aufregenden Experiment mitzuwirken.

An dieser Stelle würde ich auch noch gerne meinen Kollegen am Stefan Meyer Institut für aufschlussreiche Diskussionen und interessante Gespräche danken. Speziell möchte ich mich bei Doris Pristauz-Telsnigg, Leopold Stohwasser, Mark Pruckner, Herbert Schneider, Julia Matejka, Angela Gligorova, Markus Fleck und Andreas Pichler bedanken. Ohne ihre tägliche Arbeit und Hilfe wäre diese Diplomarbeit nicht möglich gewesen.

Den mit Abstand größten Dank muss ich meiner Familie aussprechen. Ganz besonders meinen Eltern, Yvi und Helmut, meiner Schwester Sarah und meinen Großeltern. Ihre bedingungslose Unterstützung hat mein Studium erst ermöglicht.

Abschließend möchte ich mich noch bei meinen Kommilitonen und allen Personen, die ich während des Studiums in Österreich und in den Vereinigten Staaten kennengelernt habe, bedanken. In meiner Zeit als Student habe ich viel mehr als nur Freunde fürs Leben gefunden. Ihre Beiträge, offene Ohren und enorme Unterstützung haben mein Studium zum bisher schönsten Abschnitt meines Lebens werden lassen.

Contents

1	Motivation	1
2	Introduction	3
2.1	AEgIS	3
2.2	Introduction of the Detector Components	6
2.2.1	Caesium Iodide	6
2.2.2	Silicon Photomultiplier	8
2.3	Detection of Antiprotons with a Caesium Iodide Detector	12
2.3.1	The Set-up	12
2.3.2	The Results	13
3	Preparation for a first experimental Set-up for a cryogenic Caesium Iodide Detector	17
3.1	Silicon Photomultipliers, Preamplifiers and Filters	17
3.2	Preparation and Set-up Components	19
4	Characterization of low Temperature Caesium Iodide Crystals with Room Temperature Silicon Photomultipliers	22
4.1	Light Guides	22
4.2	Set-up for a Characterization of low Temperature Caesium Iodide Crystals	24
4.3	Results of the Characterization of low Temperature Caesium Iodide Crystals	25
4.3.1	Spectra of the radioactive ^{22}Na Source taken with a cryogenic Caesium Iodide Detector	25
4.3.2	Waveforms of a low Temperature Caesium Iodide Detector using a radioactive ^{22}Na Source	28
5	Comparison of low Temperature Waveforms and Spectra of Csl and LYSO Crystals	31
6	Low Temperature Behaviour of a Silicon Photomultiplier	40
6.1	Experimental Set-up for a low Temperature Scintillator-independent Characterization of a Silicon Photomultiplier	40
6.2	Waveforms of Silicon Photomultipliers at low Temperatures	42
7	A cryogenic Caesium Iodide Detector for gravitational Measurements on Antihydrogen	49
7.1	A low Temperature Caesium Iodide Detector Set-up	49
7.2	Spectra and Waveforms of a low Temperature Caesium Iodide Detector . .	49
8	Final Test of the cryogenic Caesium Iodide Detector	58
8.1	Set-up for the final Test at the GRACE Beam line at CERN	58
8.2	Identification of antiproton annihilation signals	59

9 Discussion and Outlook	62
Appendix: Datasheets of the Silicon Photomultipliers	64
List of Figures	76
References	80

1 Motivation

It is believed that the comparison of the properties of antimatter and matter might lead to insights into one of the biggest unsolved problems in modern physics: the Baryon asymmetry. Many current experiments are now looking for differences in antimatter and matter [1, 2, 3, 4, 5, 6]. Their results might lead to an explanation of this phenomenon. One of them, trying to help understand the events of the early universe, is AEGIS [1].

The main goal of the AEGIS collaboration (Antihydrogen Experiment: Gravity, Interferometry, Spectroscopy) at CERN is the direct detection of the acceleration of an antihydrogen beam in Earth's gravitational field. The beam will transverse a device, which is highly sensitive for acceleration measurements: a Moiré deflectometer [7].

Up to now, only indirect experimental evidence and one direct measurement with antihydrogen done by ALPHA exists [8], which suggests that the Weak Equivalence Principle also holds for antimatter, a direct experimental measurement for antimatter with higher precision still needs to be carried out.

The AEGIS experiment will measure the gravitational effects on an antimatter beam passing through a Moiré deflectometer. By the use of an emulsion detector combined with a silicon-strip detector, the goal is to determine \bar{g} (the gravitational acceleration) of antihydrogen atoms with an initial relative accuracy of 1% [1]. The experiment is explained in more detail in the next section.

Since many experimental challenges lay on this way, a first and faster approach to measure the sign of the gravitational acceleration of antihydrogen was suggested. The result of the measurement will have a relative precision of 30%, this way a null result is excluded with 3σ . The concept still relies on a three-gratings Moiré deflectometer, the phase shift of the antiatoms however, will be obtained via rotation of the deflectometer. This method has already been used for the first direct detection of gravitational acceleration of neutrons in a neutron interferometer [9]. No time-of-flight information, no ultra cold, pulsed antihydrogen beam, nor a position resolution is required for this measurement. A first successful result would lead to a great step towards the long-term goal of AEGIS.

This diploma thesis introduces a possible cryogenic detector to measure the signals behind the third grating in ultra high vacuum, which allows the determination of the sign of antimatter's gravitational acceleration.

2 Introduction

2.1 AEgIS

AEgIS (Antihydrogen Experiment: Gravity, Interferometry, Spectroscopy) primary scientific goal is the direct measurement of the Earth's gravitational acceleration \bar{g} on antihydrogen. Representing the world's first direct measurement of the Earth's gravitational effects on an antimatter system would make this result scientifically relevant. In a first phase a gravity measurement with 1% precision is supposed to be carried out by sending an antihydrogen beam through a classical deflectometer coupled to a position sensitive detector. A second phase includes CPT spectroscopy in the long term scientific goal and of course higher precision gravity measurements [1].

The principle of universality of free fall has been tested for matter with very high precision [10, 11] but never before for antimatter. The principle (also known as Weak Equivalence Principle, short WEP) states that all bodies, independent of their mass and composition, fall with the same acceleration. Gravity, a classical theory which does not imply the existence of antimatter, is described by General Relativity. It is widely expected that the gravitational interaction of matter and antimatter should be identical. However, in literature a multitude of predictions appear, which are based on theoretical assumptions or indirect tests. They show a relative difference of $\Delta g/g$ between 10^{-13} and 200% (which would lead to antigravity $\bar{g} = -g$) [12]. A difference between matter and antimatter would of course violate the WEP, a cornerstone of General Relativity, but would be consistent with CPT conservation. An experiment using charged antiparticles would be very difficult because the gravitational force is much weaker than the Coulomb force. That makes electrically neutral antihydrogen an ideal probe and a unique system, with which the WEP can be directly tested.

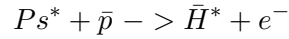
Antihydrogen consists of an antiproton (\bar{p}) and a positron (e^+). The antiprotons will be directly delivered from the Antiproton Decelerator (AD) [13, 14], which is a unique machine that produces low-energy antiprotons for studies of antimatter. A proton beam from the Proton Synchrotron is fired into a block of metal. These collisions create a multitude of secondary particles, including lots of antiprotons. The produced antiprotons have too much energy to be of use to form antiatoms so the job of the AD is to tame them and to turn them into a useful, low-energy (around a tenth of the speed of light) beam.

The positrons on the other hand will be emitted by a ^{22}Na source and accumulated in a trap. The accumulator traps and cools the continuous beam of positrons. In 200-300 seconds more than 10^8 positrons are expected to be accumulated [1].

A simple representation of the proposed scheme of the experiment can be seen in Fig. 1.

The proposed production of antihydrogen in the experiment of the AEgIS collaboration

is based on the charge exchange reaction between antiprotons and Rydberg positronium (Ps^*) [1] :



One of the main advantages of this reaction is the very large cross section, which scales with the power of four of the principal quantum number of the positronium (the cross section would be smaller for direct antiproton positron mixing). Furthermore, the expected distribution of the quantum states of the produced antihydrogen is known and their range is reasonably narrow, because it is strictly related to that of the incoming positronium. In addition, it is possible to form a beam thanks to the sensitivity of electric field gradients of the produced Rydberg atoms by accelerating them in a time depended inhomogeneous electric field.

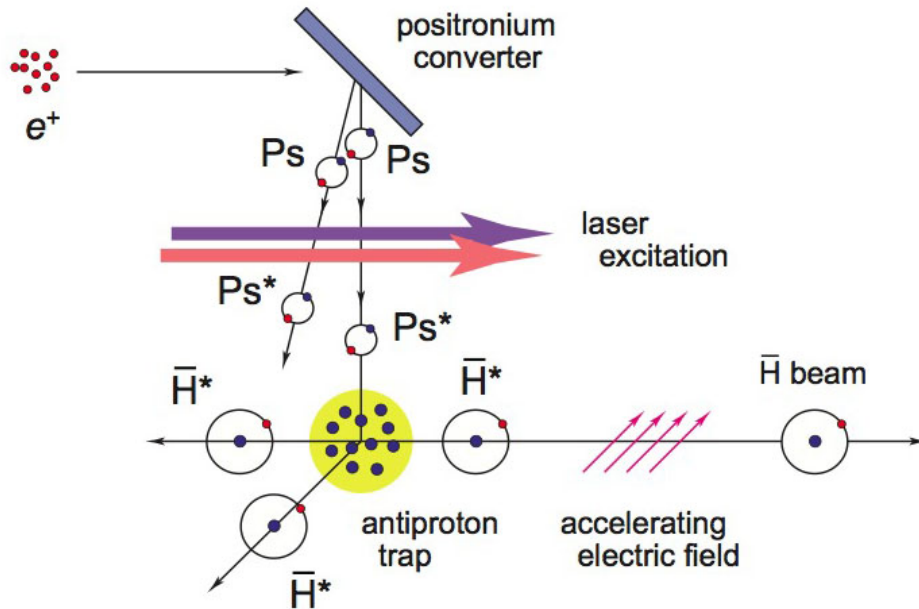


Figure 1: Simple representation of the AEGIS scheme taken from the AEGIS collaboration's website.

The positronium for this reaction is usually produced by implanting positrons with kinetic energies of the order of several hundred eV up to keV into a solid target. The target chosen for AEGIS is a nanoporous insulator (pore sizes are typically of the size of 0.3 to 100 nm) [1]. The incident positrons will be slowed down in the target and under certain conditions bond with a valence electron. The positronium produced this way will lose more and more kinetic energy by collisions and eventually leave the target (or annihilate).

The positroniums are now accumulated with the earlier accumulated antiprotons, which should lead to the production of antihydrogen. However, this reaction alone has a very low probability because the positronium is too tightly bound in the ground state. To reduce the binding energy the positronium is excited by lasers to higher quantum numbers, to form a so called Rydberg state. Quantum numbers of 30 to 40 are desired because the probability of antihydrogen production increases with the fourth power of the quantum number as stated earlier.

Since the produced antihydrogen is not electrically charged, it might leave the trap in any direction. Some of them towards the detector, where they are accelerated due to an electric gradient (antihydrogen has an electric dipole moment). A beam of around $v_h \sim 400$ m/s is formed which is crucial for the final measurement.

The beam is now entering a classical Moiré deflectometer, which is a device with high sensitivity for acceleration measurements. A classical deflectometer is usually made of three gratings, but the slit widths are sufficiently large that diffraction can be neglected. The motion of the atoms through the deflectometer is purely classical. A multitude of theoretical analyses of the inertial sensitivity of matter wave interferometers have been made, and all give the same result and predict a phase shift $\Delta\phi_g$ due to the acceleration of gravity g equal to:

$$\Delta\phi_g = k \cdot g \cdot T^2$$

where T is the time spent by the atom between consecutive diffraction gratings and k is the grating wave vector. [1]

The system of gratings splits the antihydrogen beam and produces a periodical structure in the number of the antihydrogen atoms $N(x)$ arriving at the third grating, where they will annihilate. x is pointing in the direction of the gravitational force. Gravity induces a phase shift in $N(x)$, which can be seen as the atom beam's deflection during the flight between the two gratings, exactly given by the equation above.

The deflectometer's significant advantage is that a perfectly collimated monoenergetic beam is not needed for a gravity measurement.

Instead of the third grating the upgraded design proposes the use of a position sensitive detector. The very precise position sensitive detector combines silicon strips and photographic emulsion plates. The silicon strips will allow to measure the approximate point of annihilation of the antihydrogens together with the time of arrival of each atom. To measure the annihilation points with an even higher precision, the photographic emulsion plates will be used. By looking at the annihilation pattern, this combination of detectors allows to simply measure the drop of the antihydrogen atoms of different velocities during their horizontal flight (also relative to beams of light, which do not drop on this scale). Therefore, it is simple to determine the strength of gravity between the antihydrogen atoms and the Earth.

2.2 Introduction of the Detector Components

2.2.1 Caesium Iodide

Caesium Iodide (CsI) is the ionic compound between Caesium and Iodide . CsI's most important application at room temperature is the use in electromagnetic calorimeters at high counting rates in experimental particle physics. The main advantage is that pure CsI is a fast and dense material with good light yield. Undoped CsI has its emission maximum at 310 nm at room temperature (and 340 nm at 77 K). The intensity is much smaller (a tenth) than either of the activated types (CsI(Tl) and CsI(Na)) of this material, which are one of the brightest scintillators known [15]. However, the emission of CsI is characterized in a short decay time (16 ns) which makes it useful for fast timing applications. There is also a slower component with a decay time of around 1000 ns with a maximum emission wavelength of 500 nm. This component represents only 20% of the total light. Cooling of the CsI crystals to temperatures of around 80 K increases the total light yield by about a factor of 10, however it reduces the faster component [16]. Due to the high density and the high atomic number, the crystalline solid material has a very good stopping power. This fact, in combination with the quite good radiation hardness makes CsI crystals very useful for high energy physics as well.

The temperature dependence of the light emission and the decay times for pure CsI have been measured with silicon photomultipliers (Hamamatsu R1464) and photodiodes (SINTEF) from 77 K - 295 K by Amsler et al. in [17]. Polished pure CsI crystals was used by them, wrapped in white reflecting teflon tape (higher light output) and mounted in a vacuum chamber where it was cooled down to liquid nitrogen temperatures (77 K). The light yield measurements were made using the 511 keV and the 1275 keV γ -rays from a radioactive ^{22}Na source. Fig. 2 shows the light yield dependence for a temperature interval of 80 K - 300 K. The two curves represent the light detected by the photodiode and the photomultiplier, respectively. It is easy to see that those are in good agreement. By cooling down the crystal to 77 K an increase in light yield by a factor of 15.8 was observed.

$$\frac{N_{\gamma}(77 \text{ K})}{N_{\gamma}(295 \text{ K})} = 15.8 \pm 1.0$$

Those light yields are comparable to the yields of activated types like CsI(Tl) at room temperature. In addition to the high light yield it is also important to mention that a good energy resolution of $\Delta E(\text{FWHM})/E = 8.3 \%$ for 511 keV γ -rays was obtained.

The decay time of the light produced by the pure CsI was measured with the photomultipliers in the same temperature range as above. For high temperatures (192 - 295 K), two time components were observed. The main component (76 % of the total light yield) with a decay time of 192 ns and the fast component (24 % of the total light yield) with a decay time of 39 ns are shown (dashed curves) in Fig. 3a.

Below 192 K just one component with a long decay time of about 1 μs was found (Fig. 3b). Fig. 4 shows the increase of decay time over decreasing temperature.

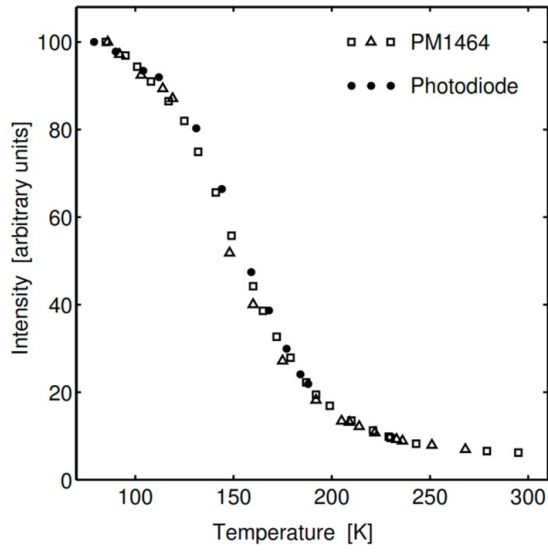
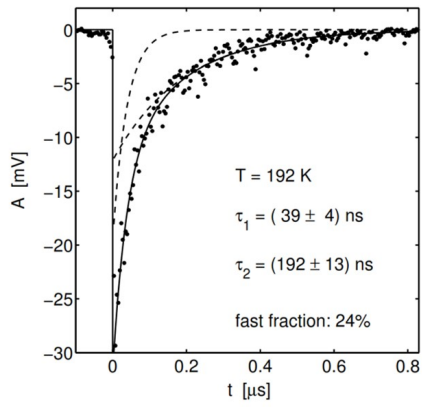
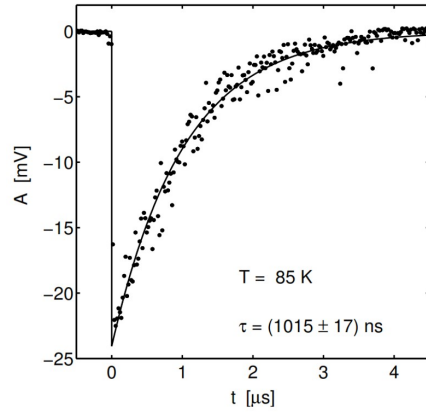


Figure 2: Light yield of pure CsI crystals as a function of temperature read out by a photodiode and a photomultiplier [17].



(a)



(b)

Figure 3: Light emission waveform for a pure CsI crystal at 192 K (a) and 85 K (b), measured with a photo-multiplier [17].

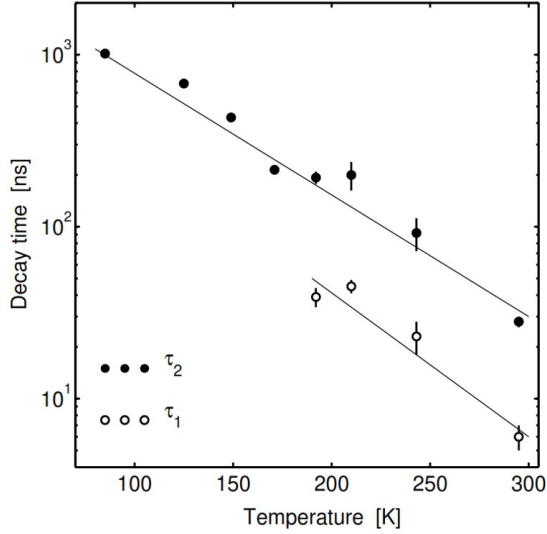


Figure 4: Decay times of the light emission for a pure CsI crystal at different temperatures [17] .

To sum up the CsI is, because of its two fast decay components, a fast scintillator at room temperature. However, the light yield is only 5% of the light yield of CsI(Tl) of comparable size. By cooling down the CsI to temperatures of liquid nitrogen the crystals become comparable in light yield of those of activated CsIs. The energy resolution at low temperatures are satisfying, however the decay time increases to 1 μ s.

2.2.2 Silicon Photomultiplier

The Silicon Photomultiplier (SiPM) is a semiconductor photodetector operated with a reverse-bias voltage well above the breakdown voltage. This mode is also known as Geiger mode and therefore the SiPM is also called a Geiger-mode avalanche photodiode (G-APD). SiPMs operated in this mode have large, well-defined output pulses because they reach intrinsic gains for single photoelectrons of 10^6 . This value is comparable to that of vacuum phototubes (PMTs) and notably higher than the gain of an avalanche photo-diode (APD). Therefore the SiPMs can be used for single photon counting.

A SiPM is a relatively inexpensive device consisting of an array of small ($\sim 20\text{-}30 \mu\text{m}$) independent pixels. Those pixels are arranged to form a macroscopic unit (500-4000 pixels/ mm^2) of 1-6 mm^2 size and are operated with a bias voltage V_{bias} a few volts above breakdown voltage $V_{\text{breakdown}}$. The photoelectrons created are reaching the high field region by diffusion or drift and start a discharge confined to that pixel. All of the independently working pixels are connected to the same readout line. The outgoing signal corresponds then to the sum of all fired pixels, which gives a measure for the light flux [18].

The many advantages of a SiPM such as high gain at low bias voltage, single photon response, high detection efficiency and very good timing properties make them of interest

for this work. The disadvantages are a high dark count rate at room temperature. However, compared to PMTs, SiPMs are considerably more insensitive to magnetic fields, which makes them a good detector for many modern experiments in high energy physics which use calorimeters in strong magnetic fields, and also at a cheaper price available.

Characteristics Of A Silicon Photomultiplier

Photon Detection Efficiency

The efficiency of a SiPM to detect photons is characterized by the overall photon detection efficiency (PDE). For SiPMs usually the quantum efficiency (QE) is used which neglects other losses. The QE is defined as the probability that one photon creates one electron-hole pair in the depleted layer of a semiconductor. Like most of the silicon based detectors a SiPM has a QE close to 90-100% for optical photons depending on the wavelength. The PDE takes a lot of other contributions into account and is a product of the quantum efficiency of the active area, a geometric factor (ϵ), and the probability that an incoming photon triggers a breakdown (P_{trigger}).

$$\text{PDE} = \text{QE} \cdot \epsilon \cdot P_{\text{trigger}}$$

The geometric factor takes losses at the entrance window into account, which can be minimized to more than 90% transmission by proper engineering of the window, as well as the ratio between active area to total area ($\sim 80\%$), which is not a 100 % due to the physical separation of the pixels.

The breakdown probability depends on the position where the electron-hole pair is generated and on the overvoltage (the electric field strength in the junction). Electrons have a higher chance to trigger a breakdown in silicon.

The last contribution to the PDE is the recovery time. It is defined as the period of time a pixel needs to recover and to be fully sensitive after a breakdown. Due to dark counts and background light around 0.1 to 1% of all pixels in a SiPM are always in recovery, which decreases the sensitive area of the detector. The recovery time depends on the pixels size due to its capacity. However the recovery time should never reach values higher than a few μs , typical values are 25 to 250 ns.

The size of the active area has the biggest impact on the PDE from all the mentioned effects. The highest reported PDEs are 40% [19]. Fig. 5 shows the PDE for present-state SiPMs in comparison with the typical QE of APDs and PMTs. For blue light the PDE for SiPMs is at the level of PMT's QE, but larger in the yellow-red wavelength-region of the spectrum [17].

Dark Counts

The electronics noise of SiPMs is very small (less than 10% of the total signal from one photoelectron) due to a very high gain. This is in contrast to the APDs where the gain is smaller. However, free charge carriers produced in the sensitive volume that reach

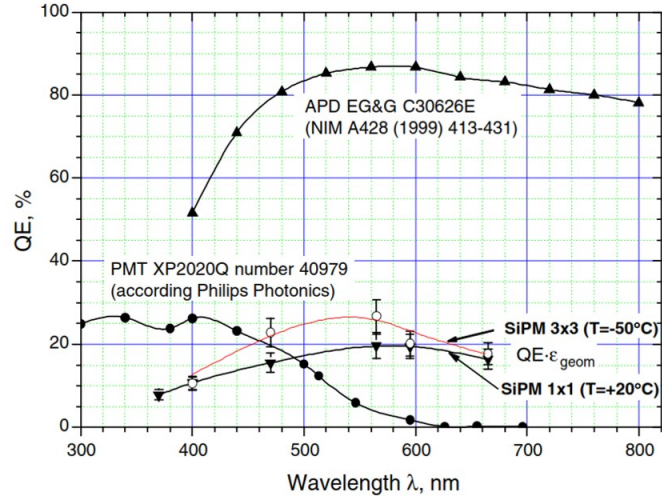


Figure 5: Comparison of the photon detection efficiency of SiPM, PMT and APD [18].

the high electric field region might lead to a breakdown. Those dark counts are mostly produced by thermally generated electrons, which limits the performance of SiPMs at room temperature for the detection of very small light signals. Current SiPMs show dark count rates of 10^5 - 10^6 per second and square millimetre of active area. By cooling of the SiPM it is however possible to reduce dark counts since thermally generated electrons will not be produced that easily. Dark counts are reduced by a factor of 2 every 8 °C. Fig. 6 shows the temperature dependence of the decreasing SiPM dark count rate for lower temperatures.

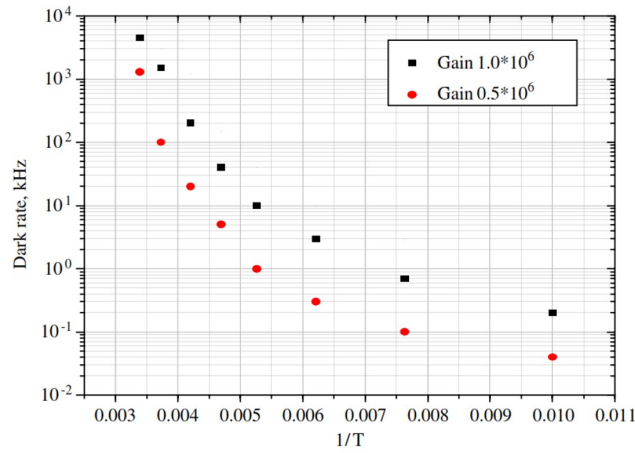


Figure 6: Temperature dependence of the SiPM dark count rate for different pixel gains [18].

High Gain

The amplitude A_i , which corresponds to the accumulated charge in the pixel, of a standard signal produced by a SiPM is proportional to the capacitance of the pixel times the overvoltage.

$$A_i \sim C \cdot (V_{bias} - V_{breakdown})$$

The overvoltage is usually of the order of a few volts and the capacitance C is typically 50 fF. A_i is of the order of 150 fC or 10^6 electrons. And when many pixels are fired at the same time the output is the sum of all the smaller signals.

$$A = \sum A_i$$

The gain is usually in the range of $10^5 - 10^7$. On a 50Ω load the signal of one pixel signal corresponds to a pulse with an amplitude of ~ 1 mV (for a typical 10-20 ns pulse length) [18, 19].

Summary

The current development of SiPMs is advancing beyond belief. There has been a lot of progress achieved in device performance, but there is still broad room for improvements. Many properties can be adjusted to optimize the devices and to make them useful for a variety of applications.

At the end of the chapter a summary of the most important properties of SiPMs, which make them such a powerful tool will be given [19]:

- Intrinsically fast response (less than 500 ps) due to a very thin depletion layer,
- short rise times,
- show little to no change when operated in a strong magnetic field,
- low operation voltage needed (< 75 V), which makes it easy to design a system with a large number of SiPMs (single coax cable is needed to supply bias voltage),
- typical dark current for a 1 mm^2 SiPM is about $1 \mu\text{A}$. Corresponding power consumption is therefore very small ($\sim 100 \mu\text{W}$),
- SiPMs with active areas of $6 \times 6 \text{ mm}^2$ are already available ($10 \times 10 \text{ mm}^2$ are planned),
- compactness,
- long term studies showed no ageing over years and a relatively good radiation hardness,
- high photon detection efficiency,

- large internal gain ($<10^5$),
- temperature and bias fluctuations are low compared to APDs,
- single photon response,
- no damage from accidental light exposure,
- low nuclear counter effect (low response to passing ionizing particles),
- easy production,
- cheap price.

The disadvantage of a high dark count rate is only a problem in applications with a low single photon count rate and can be decreased by cooling of the SiPM. Future developments will increase the photon detection efficiency over a larger range of wavelengths even further and will also make the active areas of SiPM grow in size. These prospects and the advantages listed above make the SiPM a very suitable photon detector for a wide range of applications and in some of them it is even a better choice than APDs or PMTs.

2.3 Detection of Antiprotons with a Caesium Iodide Detector

The purpose of this chapter is to quickly summarize and present the work done before at the Stefan Meyer Institute¹, on which the following chapters and consequently this work builds up.

The thesis describes the detection of antiprotons using CsI-crystals at room temperature as scintillators as well as the electronics used such as filters and preamplifiers, which produced well shaped signals and spectra. Furthermore, a simple analysis of annihilation signals was carried out.

2.3.1 The Set-up

For the final set-up three CsI crystals (17x17x13 mm³) were used. The crystals were obtained from Prof. Dr. Claude Amsler and were already used in other experiments such as ATHENA at the CERN-AD. Originally the pure Caesium Iodide crystals were bought from Saint-Gobain. For the experiment all three of them were wrapped in white reflecting thread seal tape (teflon, RS Pro White PTFE Tape, RS Stock No.512-238, thickness: 0.075 mm) and on top of the teflon, aluminium for a maximal light output. The produced light might leave the scintillator in any direction, the teflon tape helps "trapping" some of the photons in the crystal and by reflecting them onto the SiPM it increases the chances of finally detecting them. The same holds for the aluminium wrapping.

To measure the produced amount of light six NUV-SiPMs (near-ultraviolet) with an

¹Alen Lika BSc. „*The Detection of antiprotons with a CsI-Detector*“, University of Vienna

active area of $4 \times 4 \text{ mm}^2$ from AdvanSiD (ASD-NUV4S-P) were used. Two SiPMs were coupled to one of the $17 \times 17 \text{ mm}^2$ sides of one CsI, respectively, using silicon grease (BC-630 Silicone Grease from Saint-Gobain), which worked as a light guide to increase the coupling between the scintillator and the SiPM. The opposite $17 \times 17 \text{ mm}^2$ side will be facing the antiproton beam.

The final measurements were carried out at the GRACE beam line at CERN, which delivers low energy (1-8 keV) antiprotons to study annihilation signals in detectors [20]. To shape the signal produced by the SiPMs a simple highpass board was used (Fig. 7). Since a lot of antiprotons are expected the signals should have a super-fast fall time, a well-defined peak and to be in general narrow (small full width at half maximum). This way a pile up or a merging of signals produced by the SiPMs is unlikely.

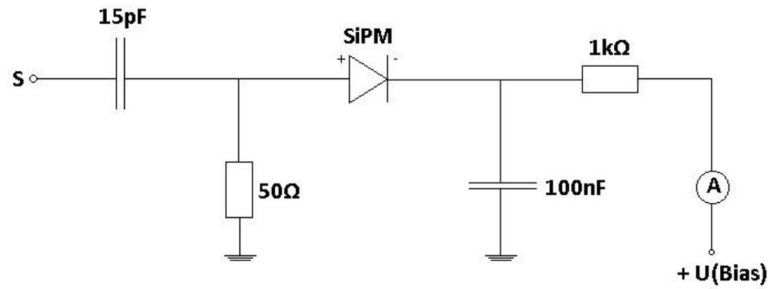


Figure 7: Schematic representation of the highpass board.

2.3.2 The Results

In Fig. 8 the waveforms recorded during a shot of antiprotons of the three SiPMs are shown. It is interesting to mention that two of the three CsIs were covered in a thin aluminium foil with only the side facing the SiPM being free of foil (the aluminium should not get in contact with the electronics of the SiPM). The third one however was not covered in aluminium foil. The reason for this was to check if there will be a difference in antiprotons detected with and without aluminium foil. The method chosen to evaluate if one peak might be from light emitted by an annihilating antiproton or not was a simple threshold and by looking at the FWHM of the corresponding peak. Narrow peaks above that threshold were identified as antiprotons, if the peak was too wide it also might have been from at least two pions due to antiproton annihilation (on average three charged pions are produced each annihilation), which pass through the scintillators at the same time. Those two cases can be seen in Fig. 8 respectively (red box and red circle).

After three antiproton beam extractions presumably 52 and 56 antiprotons were detected at the two crystals covered in aluminium foil and 74 at the one without the aluminium foil.

The work showed that this type of set-up gave a proof of principle for antiproton detection, but still leaves a lot of room for improvements. Since the final experiment will be



Figure 8: The pulse-height spectra plotted for slow antiprotons, which arrived in a time window between 2.0-2.6 μs . The three lines (blue, orange, gray) correspond to the three different SiPMs, respectively.

operated at low temperatures, it would be of interest to characterize the behaviour of the CsI crystals and the SiPMs at low temperatures as well. Also an advanced analysis of the spectra like the ones shown in Fig. 8 will be crucial, as well as a presentation of alternatives to CsI crystals. Furthermore, investigating thicker aluminium foils in front of the CsIs or even silicon wafers (since they are proposed for the deflectormeter) to stop antiprotons in the foils in front of the CsI will be of interests for the final experiment. With the right thickness of aluminium foil it should be possible to stop most of the antiprotons. Comparing the signals produced with and without the shield blocking the antiprotons, would make it simple to identify the real antiproton signals.

3 Preparation for a first experimental Set-up for a cryogenic Caesium Iodide Detector

3.1 Silicon Photomultipliers, Preamplifiers and Filters

Silicon Photomultipliers

Three different commercially available silicon photomultipliers were used in this work. In the following chapters they are only distinguished by the size of their active area. From AdvanSiD (Advanced Silicon Detectors) the ASD-NUV4S-P was used, which is a near ultraviolet (NUV) silicon photomultiplier with an active detection area of $4 \times 4 \text{ mm}^2$. From the KeTek GmbH the PM3350-EB and the PM6650-EB were used. Again two near ultraviolet photon detectors with active areas of $3 \times 3 \text{ mm}^2$ and $6 \times 6 \text{ mm}^2$ respectively. Worth mentioning is that their peak PDE is between 420-430 nm, so in a higher wavelength range than the light produced by the CsIs. The corresponding data sheets of the SiPMs can be seen in the appendix.

Electronics

To shape and examine the signals produced by the SiPMs three different preamplifiers and filters described in the following section were used. The task and the desired waveform decided the choice of the electronic component. The first filter was already described in chapter 2.3 in Fig. 7 as a simple highpass board without any amplifiers and shapers.

Amplifier Board

The amplifier board uses a differential input signal and two serially connected amplifiers to produce large negative signals. In addition to the produced analog signal a corresponding digital time signal, with a variable width, depending on the height of the analog signal and the applied threshold will be delivered. The circuit diagram of the amplifier board can be seen in Fig. 9. $V=10$ means that this board amplifies the signal by a factor of 10.

Amplifier Board II

The combination of a highpass followed by an amplifier allowed the production of super short, large negative signals. It was hoped that the amplifier board II allows the production of short signals even at low temperatures. The circuit diagram of the amplifier board II can be seen in Fig. 10.

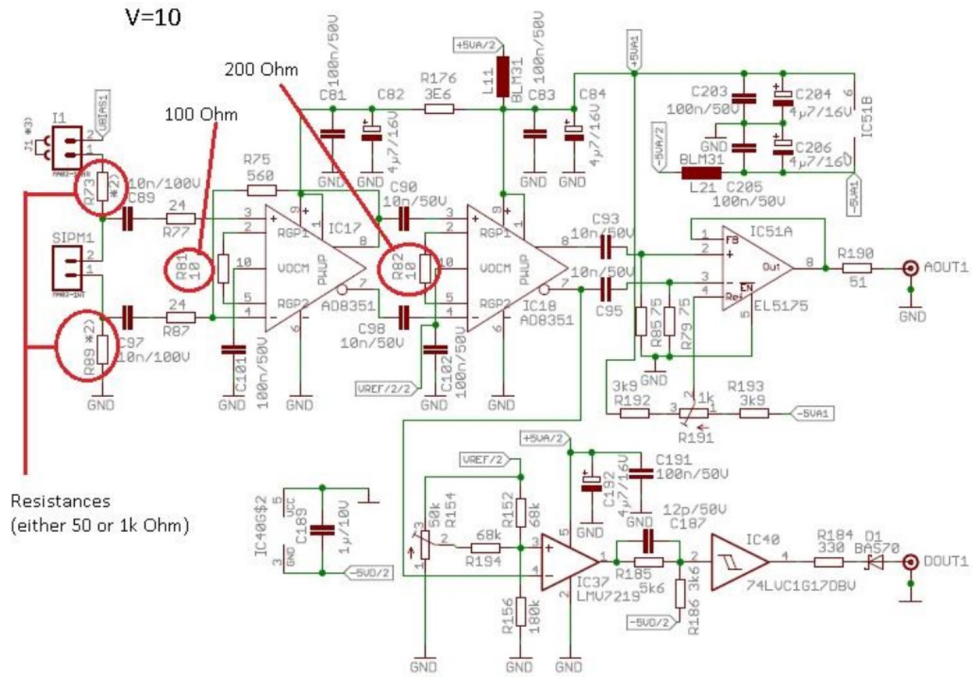


Figure 9: Circuit diagram of the amplifier board. The two red circles on the left show the differential entrance.

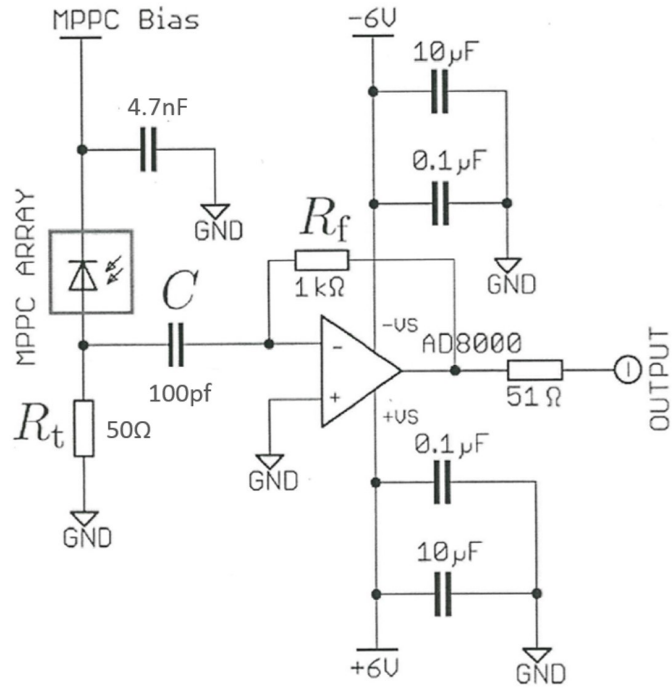


Figure 10: Circuit diagram of the amplifier board II.

3.2 Preparation and Set-up Components

The combined set-up is shown in the next section. The purpose of this chapter is to summarize the individual components of the set-up.

For a first experimental low temperature test a DN160 ISO-K cross was used to fit the set-up. Since the cooling of the CsIs and their behaviour was now of interest one of the flanges of the cross was needed to attach a cooling system and another one for the vacuum pumps.

The cooling of the detector system is accomplished by the use of a CRYOTIGER® I cooling system [21], which uses a certain refrigerant (PT14) to cool a cold-end via the Joule-Thomson-Effect. Fig. 11 shows the cooling capacity for the different refrigerants. PT14 was used and it was possible to reach temperatures of around 100 K, with a good heat conductivity even temperatures down to around 95 K.

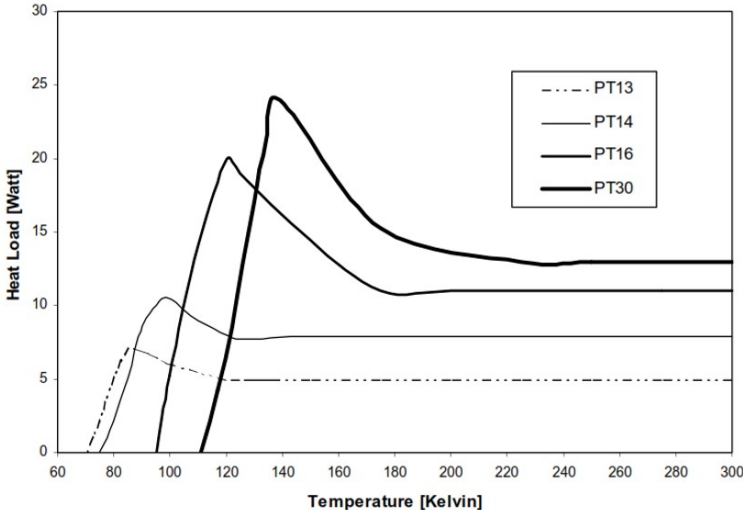


Figure 11: Cooling capacity map for the cooling system (PT14) used [21].

Only the operation of the set-up in a high vacuum environment would allow reaching temperatures described in the last paragraph. To create a vacuum of the order of 10^{-7} mbar a turbomolecular pump from Agilent (Vacuum Agilent Technologies, Twinstorr 84 Fs) was used and attached to the second flange of the DN160 cross.

One of the two flanges left was used for the electronics. Pins for the power sources to operate the SiPMs and to pick up their signals or to measure the change in resistance of Pt100s (used to determine the current temperature) were part of this flange. The signals were analysed with a Lecroy oscilloscope (Lecroy, SDA 760Zi-A, 6 GHz).

A kapton window was attached to the last flange. By placing a radioactive ^{22}Na source close to the outside of the window, it was possible to produce light in the cooled CsI crystals on the inside of the cross. It is worth mentioning that the distance between the

source and the scintillators was crucial. In an early set-up the crystals were placed in the middle of the cross (distance from window roughly 15 cm). With this set-up no change in count rates with and without the radioactive source were recorded. The radioactive source is a low intensity source that radiates in 4π , therefore it was important to keep the distance between the scintillator and the source as small as possible to achieve higher count rates.

With the components described above it was possible to construct a first set-up. The results and measurements of this low temperature CsI crystal detector are shown and explained in the next section.

4 Characterization of low Temperature Caesium Iodide Crystals with Room Temperature Silicon Photomultipliers

The behaviour of the silicon photomultipliers at low temperatures has not yet been examined and also the corresponding data sheets did not contain any information about it. To characterize the scintillator at low temperatures a first approach would be to keep the SiPMs at room temperature while cooling the CsI crystal separately. Therefore contributions and changes in the behaviour of the SiPMs at low temperatures can be avoided and solely the changes in properties of the CsI can be examined. To accomplish this it was important to find a light guide that would guide the produced light from the scintillator to the photon detectors, without conducting heat (which would result in a cooling of the SiPMs).

4.1 Light Guides

Three different types of light guides were taken into consideration:

PMMA (Polymethyl methacrylate) Light Guide Pyramid/Cone

The base of the pyramid, as shown in Fig. 12, facing the bigger CsI crystal (blue square) at low temperatures and the other side of the cut-off pyramid (light gray) focussing the collected light onto the silicon photomultiplier at room temperatures (dark gray) would have been an option worth testing, however it was not possible to find an acrylic light guide operating at wavelengths below 400 nm. Below 360 nm the bulk absorption becomes dominant and the material does not transmit light anymore (Fig. 13) [22]. Since the light produced by CsI is between 310 to 340 nm depending on the temperature, PMMA does not work as a light guide for those wavelengths.

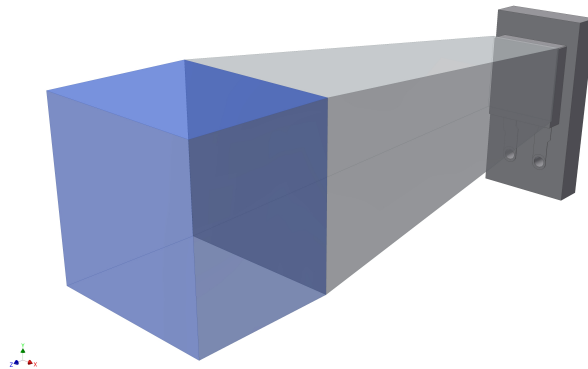


Figure 12: Set-up idea for testing the PMMA light guide pyramid. The light gray pyramid represents the PMMA.

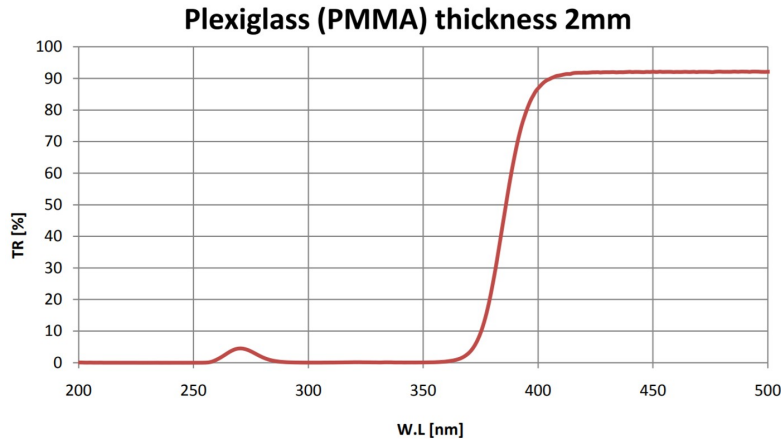


Figure 13: Transmission curve of a 2 mm thick PMMA sample in air [22].

Optical Fibers

More promising seemed the use of optical fibers (600 μm 0.22 NA UV/VIS Fiber) from Edmund Optics. Not only are they applicable in a wide range of temperatures ($-190\text{ }^\circ\text{C}$ to $390\text{ }^\circ\text{C}$), which makes them fit for use at low temperatures as well, but also do they guide and transmit ultraviolet wavelengths (Fig. 14).

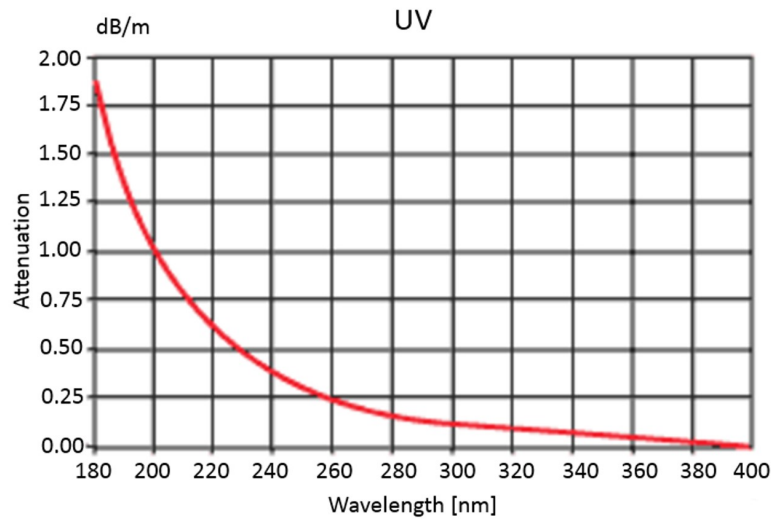


Figure 14: Attenuation for ultraviolet wavelengths for the optical fibers used [23].

To test their light transmission the fibers were cut in nine identical 30 cm long light guides. Arranged in a square, one side of the fibers (gray lines) was facing the SiPM ($3 \times 3\text{ mm}^2$ KeTek) and the other side a small $7 \times 7 \times 6\text{ mm}^3$ CsI crystal (little blue square) (Fig. 15). The diameter of the fibers including the cladding was around one mm. The side facing the crystal was more spread out with spacing

between the fibers to cover a larger surface of it. The side facing the SiPM however, was focussed with no spacing between them, which nearly covered the whole active area of the detector. The scintillator was covered in teflon tape with only the side facing the fibers being free of it. Silicon grease was used to connect the fibers to the SiPMs as well as to the scintillator.

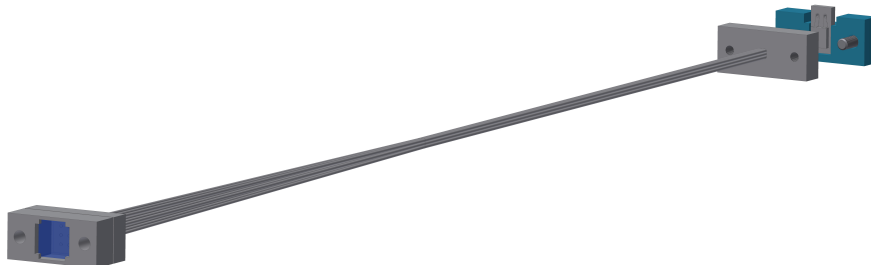


Figure 15: Set-up for optical fibers as light guides. The small blue square in the front represents the CsI, the gray lines are the nine 30 cm long fibers guiding the light to the SiPM in the back.

The whole set-up was put into a box to prohibit light from the surrounding from oversaturating the silicon photomultiplier. ^{137}Cs was used as a radioactive source to produce scintillation light in the CsI, when placing it close to the end of the box where the crystal was located. The SiPM was connected to the amplifier board (with an amplification of $V=10$) and the count rates of the signals were measured by the oscilloscope. After two ten-minute runs ($\sim 2.5 \mu\text{A}$ running through the SiPM) the count rates between with and without a radioactive source near the scintillator (1058.5 ± 23.5 to 859.5 ± 6.5) were compared. The increase in count rates by 20% showed that the optical fibers guided scintillation light to the photomultiplier. This result makes them an approach of interest for the final set-up. A more quantitative analysis was not taking into consideration, since the next candidate proved to be the best and simplest option.

A Gap (Vacuum) between the Scintillator and the Photon Detector

Even though the optical fibers showed promising results a much simpler approach was finally used to characterize the low temperature behaviour of CsI-crystals. A 1-mm gap between the scintillators and the photomultipliers in high vacuum was expected to minimize the heat exchange while still having a large enough photon-coupling between the two of them. The set-up is described in the next section.

4.2 Set-up for a Characterization of low Temperature Caesium Iodide Crystals

As described in chapter 3 the distance between the scintillator and the radioactive source remained a problem. For this set-up the distance between the two of them was minimized by placing the scintillators as close as possible to the kapton window in the DN160 cross.

This made it possible to cool the scintillators on the inside of the cross while having the radioactive source outside and therefore also removing the radioactive source was simple now.

The set-up is shown in Fig. 16 and Fig. 17. Three big CsIs ($17 \times 17 \times 13 \text{ mm}^3$) were wrapped in teflon and aluminium with only the side facing the detectors being free of it. The scintillators were put into an aluminium rectangle with a groove in the middle (big enough to fit the three CsIs) next to each other. One $17 \times 13 \text{ mm}^2$ side was facing the window (and the radioactive source) and the opposite side was facing the detectors. With a thin copper sheet and plastic screws it was easy to secure them in the aluminium block, to keep them from moving and to ensure a good heat contact between the scintillators and the aluminium block.

The aluminium rectangle was connected to the cold-end via two thick copper wires on the top and the bottom of the rectangle. To increase the heat exchange between the copper wires and the aluminium rectangle a thermal conductive grease was used. So by cooling the cold-end the heat from the rectangle and the CsIs was slowly removed. The SiPMs (three double $6 \times 6 \text{ mm}^2$ KeTek, one for each CsI) however, were attached to the rectangle via plastic screws and a plastic mounting with a 1 mm distance between them and the cold CsIs. They were attached to the plastic mount with a double-sided tape. Two metal rods connected to the aluminium rectangle on the left and the right side via two plastic mounds (almost no heat transfer) prevented the rectangle from getting into contact with the DN160 cross. The other side of the metal rods was connected to the port of the cross opposite to the window's flange. The pins for the electronics were located at this flange. Four Pt100 were used, one in contact with the cold-end and another one in contact with the aluminium rectangle itself, monitoring the change in temperature of the scintillators. To double check, the third Pt100 was in direct contact with one CsI (the Pt100 was put on the top of the CsI between the teflon and the CsI itself) and the last one was placed (in a later test run) at the position of one of the photomultipliers (this SiPM was removed from the set-up and the Pt100 was able to display the change in temperature of the SiPMs).

4.3 Results of the Characterization of low Temperature Caesium Iodide Crystals

4.3.1 Spectra of the radioactive ^{22}Na Source taken with a cryogenic Caesium Iodide Detector

^{22}Na decays by emitting a positron (β^+ decay) into excited ^{22}Ne . The excited neon state passes into the ground state whereby a 1275 keV γ quantum is emitted. The annihilation of the emitted positrons with electrons from the surrounding matter produces the characteristic annihilation photons (two 511 keV photons). Plotting histograms of the peak heights of the SiPM-signals over a certain period of time would give spectra, characteristic for the decays of ^{22}Na . Even though the resolution of the oscilloscope was high, the processing time was too long to resolve the 511 keV peak as well as the 1275 keV peak. Therefore the signals were fed into an ADC (CAEN, DT5780, Dual Digital Multi

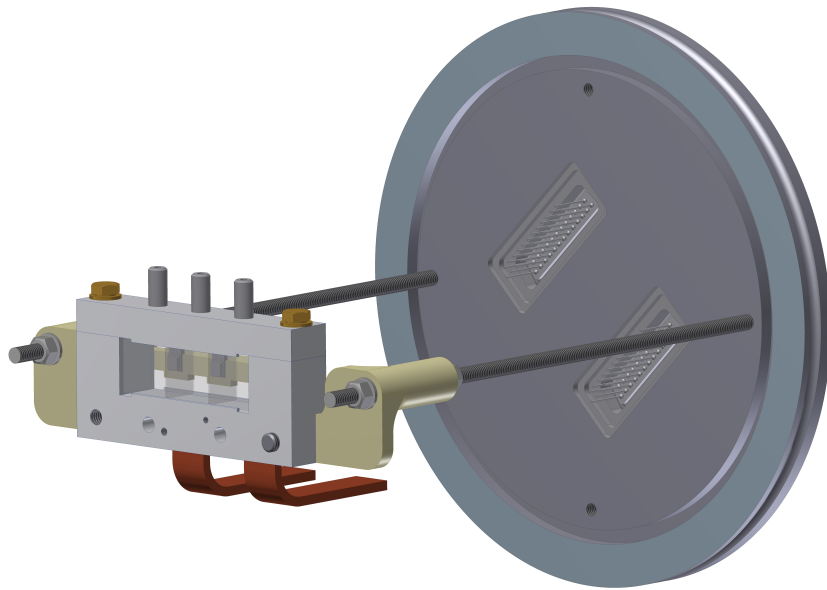


Figure 16: The set-up used to check if a gap between the scintillators and the silicon photomultipliers would guide a sufficient amount of light to the photomultipliers. The front view shows the gray aluminum block containing the CsI crystals in the middle. The copper wires on the bottom are connected to the CRYOTIGER® I cooling system, responsible for the heat transfer. The two plastic mounts on the left and the right are connecting the whole set-up to the metal rods. In the back the flange with the pins for the electronics' lines can be seen.

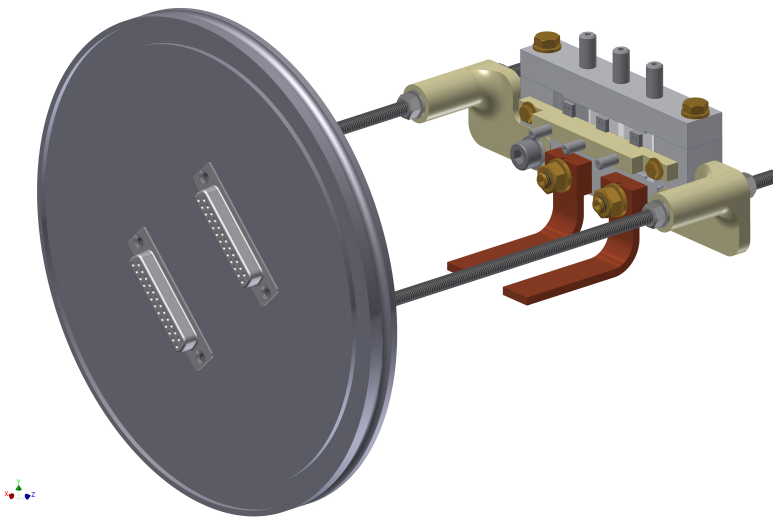


Figure 17: Back view of Fig. 16. In the back the mount (beige) for the SiPMs can be seen.

Channel Analyzer) and with the corresponding software (MC²-Analyzer) it was possible to plot the spectra with a good resolution. To process the SiPM signal the amplifier board (with an amplification of $V=3$) was used.

After the cooling was started the change in temperature was recorded and is shown in Fig. 18. While the scintillators cool down to temperatures of -150 °C the photon detectors stay at around -10 °C. No drastic changes in properties are expected for the silicon photomultipliers at those temperatures (only less dark counts). With calibrated temperature sensors the temperature of the aluminium block (blue line) should be lower than the temperature of the scintillators (green line). So the small difference of a few degrees here is due to a lack of calibration. The temperatures were achieved in a high vacuum of $5 \cdot 10^{-7}$ mbar.

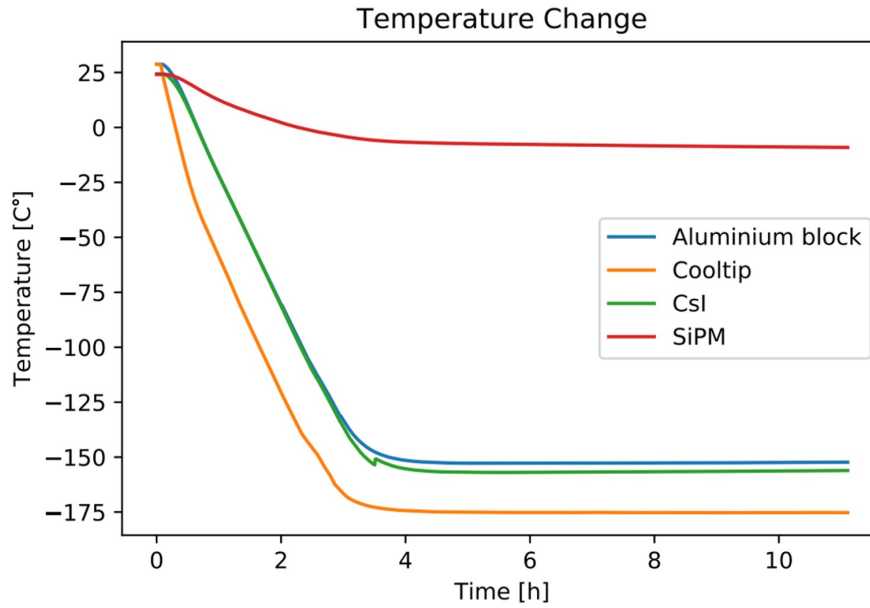


Figure 18: Change of temperature in the DN160 cross recorded at different positions. While the scintillators cooled off the SiPMs stayed relatively warm.

The first recorded spectrum can be seen in Fig. 19. It was recorded overnight for 16.5 h and shows the characteristic decay spectrum of ^{22}Na . The big peak in the middle corresponds to the full-energy peak of 511 keV annihilation photons and the smaller (higher energy results in a smaller cross section for the photons, hence a longer compton tail and a smaller full energy peak) one in the right of the figure corresponds to the full-energy peak of 1275 keV photons emitted when Ne passes into the ground state. The big peak on the left of the figure shows the compton edge of photons, that scatter in the SiPM and do not deposit all of their energy there. A current of $0.56 \mu\text{A}$ was running through the SiPM. It was possible to obtain similar spectra for all three CsI detectors. The current applied to the SiPM changed the position of the peaks in the spectrum (higher currents result in a higher gain, producing larger peak amplitudes, which shift

the spectra to the right of the graph). There was no energy calibration carried out so the x-axis shows arbitrary units (Channel numbers) instead of keV. A second 16.5 h measurement under the same conditions was carried out and the exact same spectrum was obtained, which showed that the results are reproducible. A drift in current would have resulted in higher or smaller amplitudes which would have shifted the spectra to lower/higher channels. This behaviour however was not observed, the current stayed constant for a longer period of time.

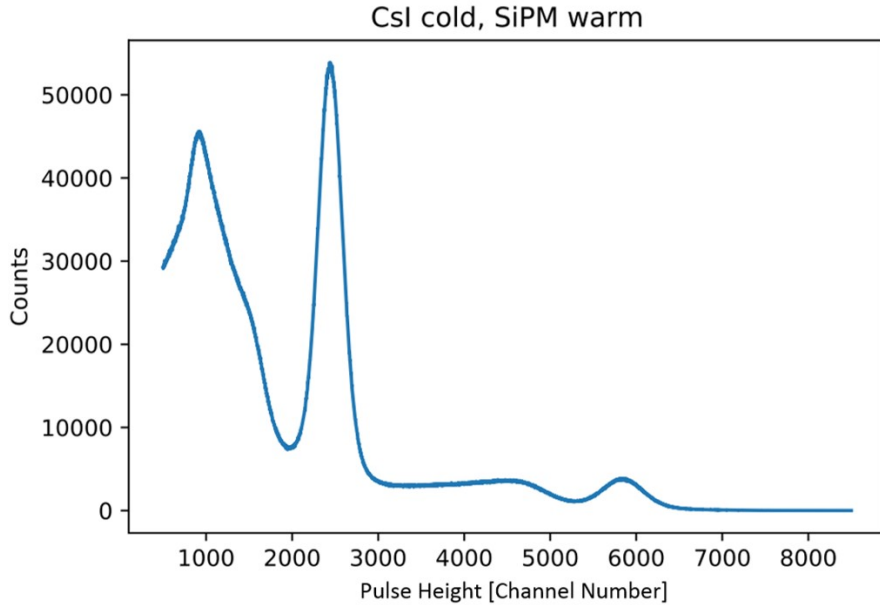


Figure 19: First spectrum recorded with the ADC with a run time of 16.5 hours. The bias voltage applied to the SiPM set the current to $0.56 \mu\text{A}$.

4.3.2 Waveforms of a low Temperature Caesium Iodide Detector using a radioactive ^{22}Na Source

The fast decay component, as mentioned in chapter 2.2.1, of the CsI crystals freezes out at low temperatures. The waveforms recorded with the cooled off set-up from chapter 4.3.1 got significantly longer (around 10 times longer decay times). Going back to chapter 2.3.2 and looking at Fig. 8 shows that longer signals would have an undesired effect: the peaks produced by the annihilation of antiprotons would overlap and there will not be a clear separation of them anymore. For the final measurement this would not result in an issue, because only five antihydrogen atoms will be expected per run (in contrast to the huge amount of pions and antiprotons).

The amplifier board II described in 3.1, which produces very short signals, was believed to narrow the cold CsI signals a little bit. In Fig. 20 a comparison of a warm (room temperature) plastic scintillator (Bicron BC-408 Premium Plastic Scintillator) signal with a cold CsI crystal signal is shown. Both signals were produced by the same SiPM and

the amplifier board II using ^{22}Na .

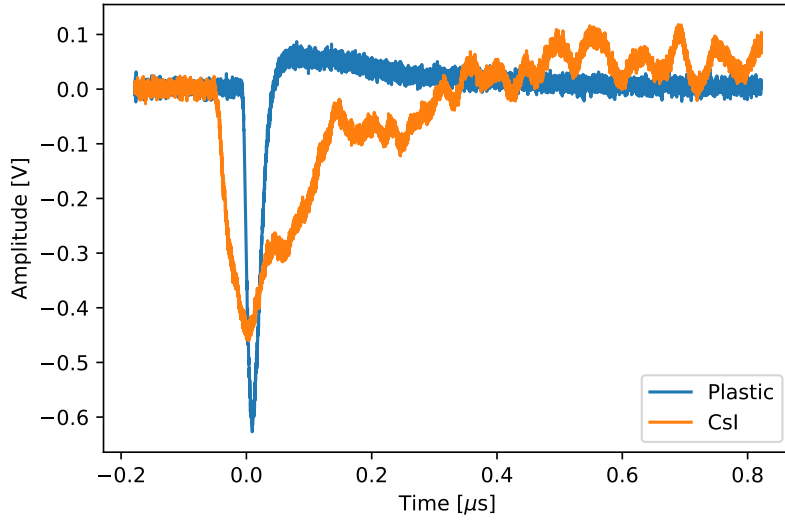


Figure 20: Comparison of a room temperature plastic scintillator signal (blue) and a cold CsI signal (orange).

It is obvious that the signal produced by the cold CsI crystal has a longer decay time. The SiPMs were still at a relatively warm temperature, so this long decay time is solely an effect caused by the CsI crystal. As the amplifier board II was optimized for pulses with fast decay times, the signal of the CsI got distorted (Fig. 20 orange line). Since short pulses are desirable for the measurements at the GRACE beam line at CERN, it is interesting to test alternatives to the CsI crystals. The next subsection introduces a new crystal, which properties show a different low temperature behaviour than the CsI. Additionally, waveforms are analysed in more detail.

5 Comparison of low Temperature Waveforms and Spectra of CsI and LYSO Crystals

LYSO ($\text{Lu}^{1.8}\text{Y}^2\text{SiO}_5\text{Ce}$) is a Cerium doped Lutetium based scintillator with similar properties as a CsI scintillator [24]. It is a high density, short decay time (41 ns) scintillator with an maximum emission wavelength at 420 nm, which makes it ideal for the SiPMs used. The light output of a LYSO crystal is ten times higher than the light output of the CsI crystals of comparable size.

The LYSOs used were again from Saint Gobain and had a total volume of $6 \times 6 \times 8 \text{ mm}^3$. To make the comparison reasonable smaller CsIs ($7 \times 7 \times 6 \text{ mm}^3$ instead of the $17 \times 17 \times 13 \text{ mm}^3$) were used. The set-up can be seen in Fig. 21. It shows a similar set-up to chapter 4.2, but instead of three CsIs it contains one LYSO crystal and one CsI crystal. Both scintillators were wrapped in aluminium and teflon tape with only the sides facing the SiPMs being free of it. One of the LYSO's $6 \times 6 \text{ mm}^2$ was facing the SiPM. Since the crystals are now smaller, only single $6 \times 6 \text{ mm}^2$ photon detectors from KeTek were used (instead of the double $6 \times 6 \text{ mm}^2$ in the previous chapter). Those were sufficient to cover nearly all of the crystal's surface, which was facing the SiPM. Again the gray block in the middle represents the aluminium block, containing the scintillators (the smaller LYSO crystal is shown on the left and the CsI crystal on the right of the figure). The copper wires can be seen at the bottom. The rods and the flange are not shown in this figure, but were the same as in the previous set-up. Besides those changes, the set-up was identical to that from chapter 4.2.

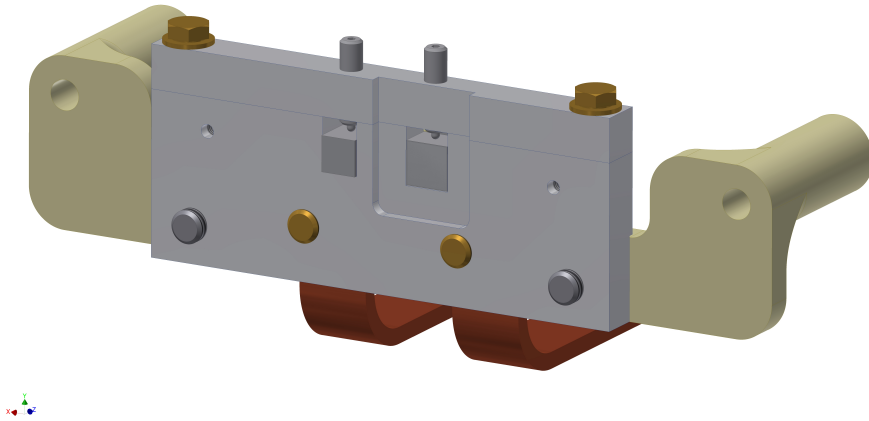


Figure 21: The set-up for the LYSO is similar to Fig. 4.2, instead of three CsI crystals a smaller CsI crystal and a LYSO crystal were used. The flange and rods are not shown in this figure.

The change in temperature of the individual parts of the set-up can be seen in Fig. 22.

Again, this graph is similar to the figure shown in chapter 4.2 (Fig. 18). The 1-mm gap between the aluminium block and the photon detector prevented them from cooling off like the rest of the set-up. The silicon photomultipliers reached temperatures of around $-10\text{ }^{\circ}\text{C}$.

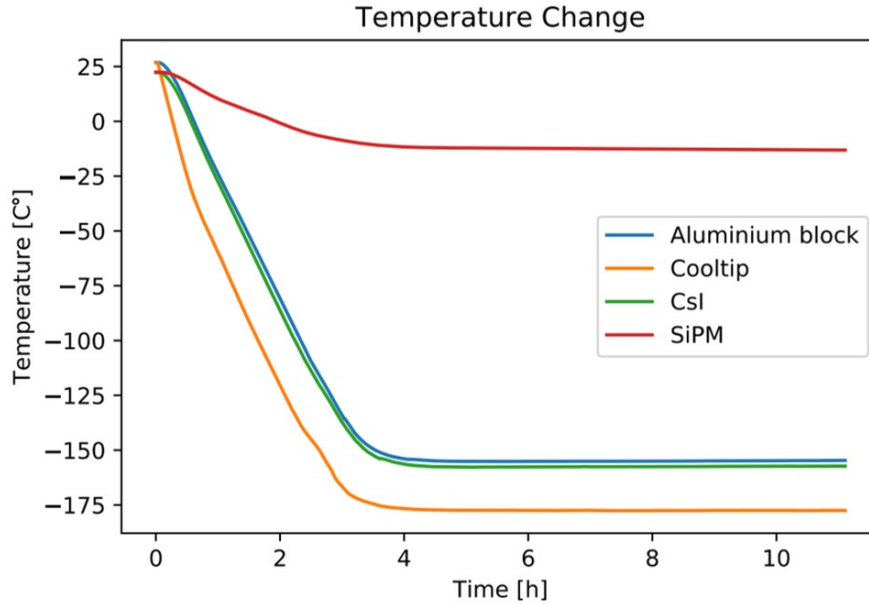


Figure 22: Change of temperature in the DN160 cross recorded at different positions for the new set-up shown in Fig. 21.

Spectra

The corresponding spectra of the radioactive ^{22}Na source were taken in a similar way to chapter 4.3.1. The signals produced by the silicon photomultipliers were again fed from the amplifier board (with an amplification of $V=3$) into the ADC, where the signals were again analysed by the MC^2 -Analyzer-software.

It is worth mentioning that the count rates as well as the amplitude of the signals produced by the LYSO were indeed higher than the signals produced by the CsI (due to the higher light output of the crystal). Since the photon detector facing the LYSO was exposed to a higher light flux less current was needed to achieve signals of comparable amplitude. To demonstrate the higher light output of the LYSO crystal spectra were taken, where a current of $0.6\text{ }\mu\text{A}$ was running through the SiPM at the LYSO-side and a current of $3.8\text{ }\mu\text{A}$ through the SiPM at the CsI-side. The spectra were recorded for a period of time of 22 hours and are shown in Fig. 23 (spectra minus the background/dark count rate).

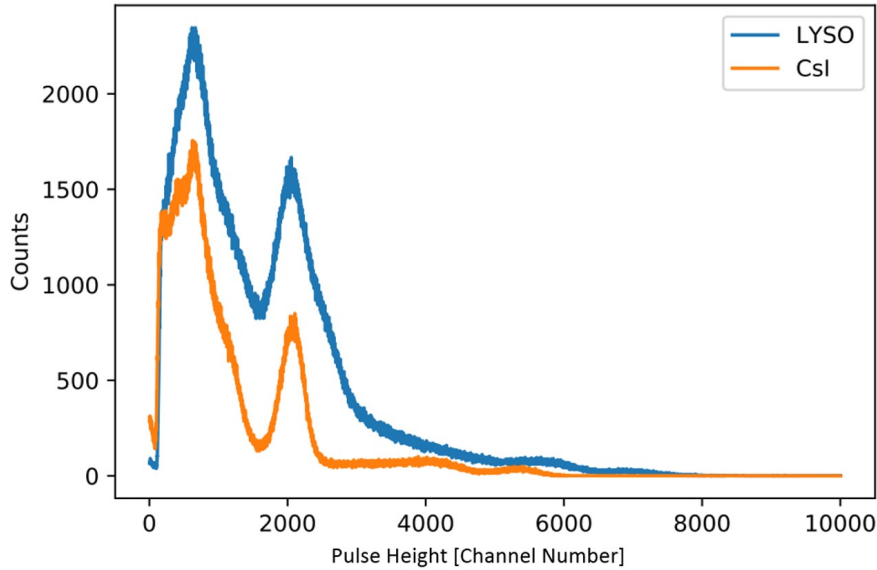


Figure 23: Comparison of ^{22}Na spectra of low temperature CsI and LYSO crystals. A current of $0.6 \mu\text{A}$ was applied to the SiPM facing the LYSO and $3.8 \mu\text{A}$ to the one facing the CsI. These spectra were the results of a 22 hour measurement.

Again, no energy calibration was carried out, which results in arbitrary units at the x-axis. However the form of both spectra was similar to the one in chapter 4.3.1. Both peaks (511 keV and 1275 keV) and the Compton edge can be seen. The 1275 keV peak is not so apparent for the LYSO-spectra, this however might be due to the settings in the MC²-Analyzer-software (not ideal settings might lead to a lower resolution).

Even though the SiPM at the CsI-side was operated with a six times higher current the signals produced by the LYSO were still larger. The current was chosen in a way that the 511 keV peak is located for both crystals at approximately the pulse height (placing them at the same spot on the x-axis). Nevertheless the count rate of the LYSO was still higher. In 22 hours 11132860 counts were detected at the CsI-side and 22595260 counts at the LYSO-side. Part of this difference of a factor of two might most likely be due to a difference in the emission wavelength. The silicon photomultipliers show a higher detection efficiency in the blue/violet part of the wavelength spectrum (LYSO emission) than in the ultraviolet part (CsI emission). However, some contribution to the difference in count rates is most likely due to a higher light yield of the LYSO as well.

Fig. 24 shows again the spectra of ^{22}Na , but now with the same current applied to both silicon photomultipliers ($1.18 \mu\text{A}$) after a 30 minute measurement. It is easy to see that the produced signals at the CsI side are smaller in amplitude than the signals of the LYSO. The difference in count rates was now higher than in the previous case, where a higher current was applied to the CsI-SiPM (200 000 to 500 000 counts respectively). The higher current and therefore the higher over-voltage made it easier to trigger a breakdown in the SiPM and hence resulting in a higher count rate.

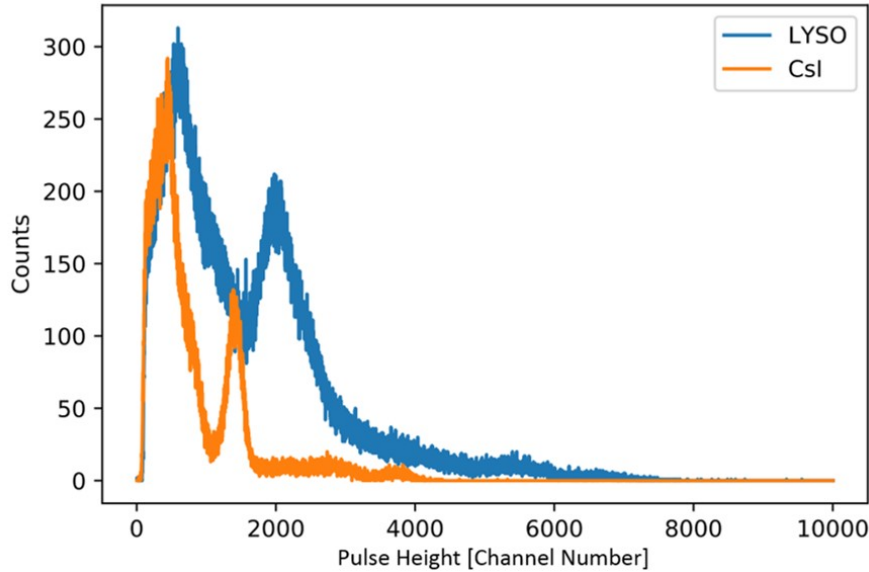


Figure 24: Comparison of ^{22}Na spectra of low temperature CsI and LYSO crystals. A current of $1.18 \mu\text{A}$ was applied to both SiPMs. These spectra were the results of a 30 minute measurement.

Since the LYSO was also able to reproduce the decay spectrum of a radioactive ^{22}Na source with a reasonable resolution, it might be a promising alternative to the CsI scintillator. In the next subsection the corresponding waveforms at low and at room temperatures are examined.

Waveforms

With the scintillators at low temperatures (around $-150 \text{ }^\circ\text{C}$ from Fig. 22, same set-up as in last subsection) a higher light yield of the scintillators was observed (chapter 2.2.1). To produce well-defined signals a relatively low current ($\sim 0.3 \mu\text{A}$) operating the silicon photomultipliers was sufficient, however, as discussed earlier, this light yield decreases at room temperatures. So while examining the behaviour of the scintillators at room temperature relatively high currents (over $10 \mu\text{A}$) would have to be applied to the SiPMs to produce signals or to be precise to produce signals of comparable amplitudes to those at low temperatures.

With the regular highpass board (Fig. 7) it was nearly impossible to produce signals using the small CsI crystal and the ^{22}Na at room temperatures. For the LYSO on the other hand, signals were easily detected. This was due to the higher efficiency of the SiPM at the emitted wavelengths and probably due to a higher light yield even at room temperatures.

Using the amplifier board on the other hand, which was already used to record the spec-

tra (with an amplification of $V=3$) and which is described in chapter 3.1, it was possible to produce well-defined waveforms at low and at room temperatures for a first qualitative analysis. Given the form of the waveforms with a short fall time and a longer rise time, it was obvious to use a linear fit for the fall time and an exponential fit for the rise time. The signals at low temperatures reach amplitudes well above 300–400 mV for the LYSO and CsI crystals when approximately $1 \mu\text{A}$ is applied to their photon detector. But since the signals were smaller (~ 20 mV) at room temperatures the current at low temperatures was further decreased to achieve signals of comparable amplitude. For the analysis signals of -10 and -20 mV were chosen. At CERN the detection of signals of different amplitudes are expected. -10 and -20 mV were chosen to check if amplitude-dependent changes in the fall time appear and because they were still obtainable at room temperatures. Higher amplitudes would have needed a higher applied bias-voltage, which might lead to a damage of the SiPMs.

The oscilloscope described in chapter 3.2 was used to record the signals.

Fig. 25 shows the waveforms produced by the CsI at low temperatures (-150 °C) and room temperatures (20 °C). The figure shows the comparison of -10 mV signals as well as -20 mV signals. A vertical offset of $4 \mu\text{s}$ was added to the -20 mV signals to make the separation between the -10 mV and -20 mV signals clearer. The oscillation in the cold CsI signal (in red, in the right of the figure) is due to picked up Wifi signals. While the fall times of the cold waveforms nearly stay the same, as can be seen in the figure, the rise times increase. The higher noise on the warm waveforms is a result of the higher current operating the SiPMs, to achieve signals of comparable amplitude. The higher current causes the amplifier board to amplify the noise more than it amplifies it in the cold case, where a smaller current is applied.

Fig. 26 shows similar waveforms to Fig. 25, however this time for the LYSO. The figure again compares -10 mV and -20 mV signals of the scintillator at low temperatures (-150 °C) and at room temperatures (20 °C). Again a vertical offset of $4 \mu\text{s}$ was added to the -20 mV signals and the noise at the waveforms at room temperatures was higher than for the ones at low temperatures.

The low temperature behaviour of the LYSO crystal is however dissimilar. There is no slow component observed at low temperatures, the fast component does not freeze out as in the case of the CsI crystal. There was hardly any disparity between the waveforms at -150 °C and 20 °C. So even at low temperatures the waveforms of the LYSO were fast and narrow.

It is worth mentioning that a current of $8 \mu\text{A}$ was applied to the SiPM facing the CsI at room temperature to achieve amplitudes of -20 mV, for the SiPM at the LYSO side however, only $1 \mu\text{A}$ was needed. At low temperatures $0.3 \mu\text{A}$ were needed to produce signals of an amplitude of -20 mV. Which means that the light yield of the LYSO was high at room temperature and even increased when cooled off. The light yield of the CsI crystal of comparable size was low at room temperatures, but also increased, as already mentioned before, to a reasonable high light yield at low temperatures.

For the fits, as stated above, a linear fit for the fall time and an exponential fit for the rise time were chosen. Due to the form of the waveforms, a linear fit for the fall time proved to be best choice with the smallest error. A lot of waveforms were produced and

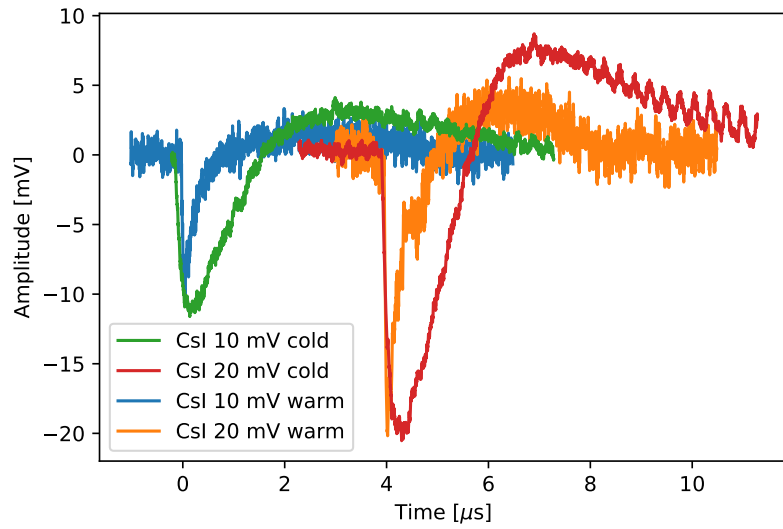


Figure 25: Comparison of signals of a cold CsI crystal ($-150\text{ }^{\circ}\text{C}$) and the signals of the CsI crystal in the same set-up at room temperatures (warm, $20\text{ }^{\circ}\text{C}$).

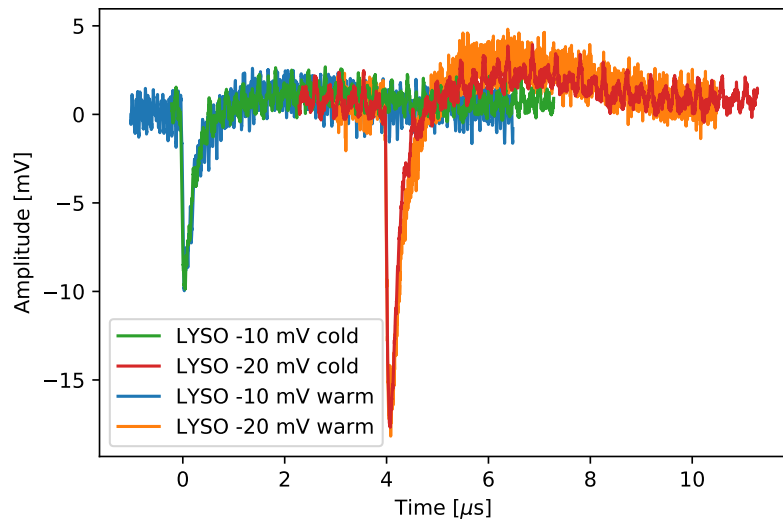


Figure 26: Comparison of signals of a cold LYSO crystal ($-150\text{ }^{\circ}\text{C}$) and the signals of the LYSO crystal in the same set-up at room temperatures (warm, $20\text{ }^{\circ}\text{C}$).

analysed. The ones shown in Fig. 25 and Fig. 26 are a random sample of them. Since no significant dissimilarity between those waveforms was found, only a few of them were used for fitting. In Fig. 27 an example of one of the fits is shown.

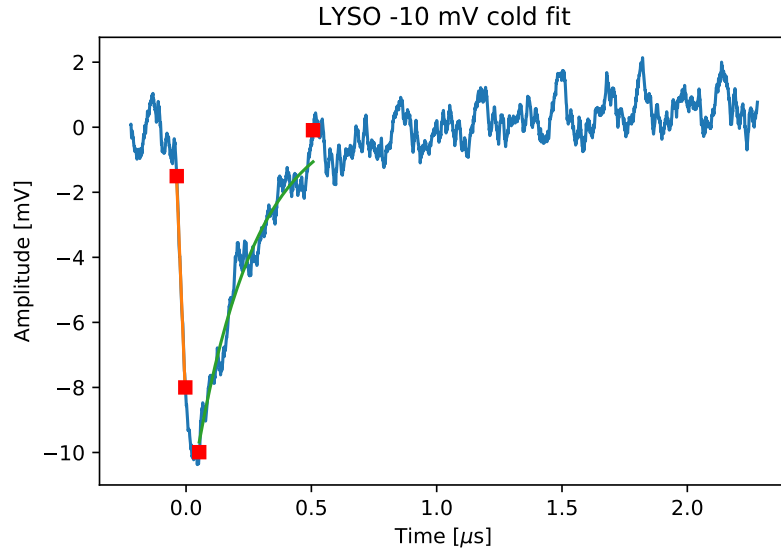


Figure 27: Waveform produced by the LYSO crystal at -150°C while $0.3 \mu\text{A}$ were used to operate the SiPM. The red squares show the start and end points of the fits. In orange is the linear fit for the fall time and in green the exponential fit of the rise time.

The start and end points (red squares) for the fit curves were chosen to be roughly 10% and 90% of the minimum of the curve (so roughly at -1 mV and -9 mV for Fig. 27). The fall time was identified as the time (x-axis) it took the signal to drop from 10% to 90% of the total amplitude (the difference in time between the red squares). For the rise time the same method was used. The orange curve shows the linear fit of the fall time and the green curve the exponential fit for the rise time. The equations used can be seen in the following ((1) & (2)).

For the linear fit:

$$y = a \cdot x + b \quad (1)$$

For the exponential fit:

$$y = a \cdot e^{-b \cdot x} + c \quad (2)$$

So by expressing x, plugging in the 10% and 90% y-values of the amplitude and forming the difference of them, the fall/rise time was obtained.

Table 1: Calculated fall and rise times for the waveforms produced by the CsI.

CsI		fall time [ns]	rise time [ns]
warm	-10 mV	51.3	599.4
	-20 mV	45.8	575.5
cold	-10 mV	115.5	964.4
	-20 mV	186.3	1141.3

Table 2: Calculated fall and rise times for the waveforms produced by the LYSO.

LYSO		fall time [ns]	rise time [ns]
warm	-10 mV	32.7	516.8
	-20 mV	56.6	520.0
cold	-10 mV	39.1	507.8
	-20 mV	59.9	558.3

Tab. 1 and Tab. 2 show the rise and fall time for the CsI and LYSO crystal respectively. The provided numbers underline the outcome, which can be seen in Fig. 25 and Fig. 26. While the fall time for the LYSO nearly stays constant for low and room temperatures, the fall time for the CsI however differs a lot. Tab. 1 shows that the fall time for the CsI increases for low temperatures, which is consistent with the freeze out of the fast component for low temperature CsI crystals.

The same holds for the rise time, here the effect for the CsI crystal is even more distinct. The rise time at low temperatures doubles when compared to rise time at room temperature, which results in a slower signal at low temperatures. Including the bigger overshoot at low temperatures the length of the signal of the CsI crystal increases by a considerable amount. On the other hand the rise time for the LYSO crystal shows no change when cooled off.

The LYSO proved to be a powerful tool. Not even did it work to take spectra of a radioactive source using a LYSO crystal as a scintillator, but also did the waveforms at low temperatures prove to be narrow and fast. Compared to the low temperature CsI signals, LYSO signals turned out to be 10 times faster. This especially would be of interest for a set-up/measurement as described in section 2.3. Here, as already mentioned, fast signals at low temperatures would be needed for a final antiproton measurement. Again worth mentioning is also the high light yield of the LYSO even at room temperatures. However, for the final antihydrogen measurement, the CsI will be used, even though the LYSO might be a better candidate. The CsI crystals have already been tested for room temperature using an antiproton beam, where they have proven their values, as they were effective in the set-up shown in chapter 2.3. At the time of the measurements larger CsI crystals were available, whereas the LYSO was not.

6 Low Temperature Behaviour of a Silicon Photomultiplier

Since the CsI set-up from chapter 4 proved sufficient and the low temperature behaviour of the CsI crystal has been characterized, the next logical step was to examine the low temperature behaviour of the SiPMs. To end up with a compact detector system, it would be an advantage to get rid of the gap between the photon detectors and the scintillators. However the combined unknown behaviour of the SiPMs and the CsI crystals would have led to questionable results. To ultimately test the low temperature properties of the silicon photomultipliers a scintillator-independent set-up would be desirable.

6.1 Experimental Set-up for a low Temperature Scintillator-independent Characterization of a Silicon Photomultiplier

In order to achieve a scintillator-independent set-up, a light source was needed to mimic the produced light by the scintillator. Using a light emitting diode and shining its light (in a reasonable intensity) directly onto the SiPMs would have the same effect as using a scintillator (with a comparable maximum emission wavelength) and a radioactive source. The idea for a simple set-up was to cool off the SiPMs facing the diode, which are kept at room temperature. This guarantees, that the properties of the diode will not change at lower temperatures and the effects observed will be merely from the change of properties of the silicon photomultipliers. Additionally, this time a heating element is added to the set-up close to the SiPMs. This way the behavior over a wider range of temperatures can be examined. A simple presentation of the SiPM's side of the set-up is shown in Fig. 28.

The copper-coloured block represents the cold-end which is connected to the front part via an aluminium bar for the heat exchange. The front part consists of a aluminium square. On the back of the square was the heating element installed, for which a simple resistor was used. Applying a current to it results in a heating of the resistor and its surrounding. The SiPM was attached to the front of the aluminum square with a plastic component (small gray cuboid in the front). The plastic component shows three holes, the two on the left and right of it are meant for the screws connecting it to the aluminium square. The hole in the middle is for the light impinging the SiPM, it was big enough to expose the active area of the SiPM to the emitted light. The back of the plastic component was hollowed out to fit the SiPM inside of it. For a better heat exchange heat paste was applied to the back of the SiPM. One Pt100 was attached to the cold-end and a second one on the aluminium square. The latter is used for the heat controller monitoring the temperature of the SiPM. The SiPM was connected to the aluminium block with silicon grease to increase the heat transfer.

The LED is at the opposite opening of the DN160 cross. On the inside of the cross the LED is separated by a distance of 8 cm from the SiPM. The pins of the LED are connected to the outside where a pulse generator (Keysight, 81160A Pulse Function Arbitrary Generator) operates it. Having a distance of 8 cm ensured that the LED would not cool off like the rest of the set-up. The light emitting diode used is from Kingbright (L-934MBCBLUE). Its peak wavelength is with 430 nm perfect for the silicon photomul-

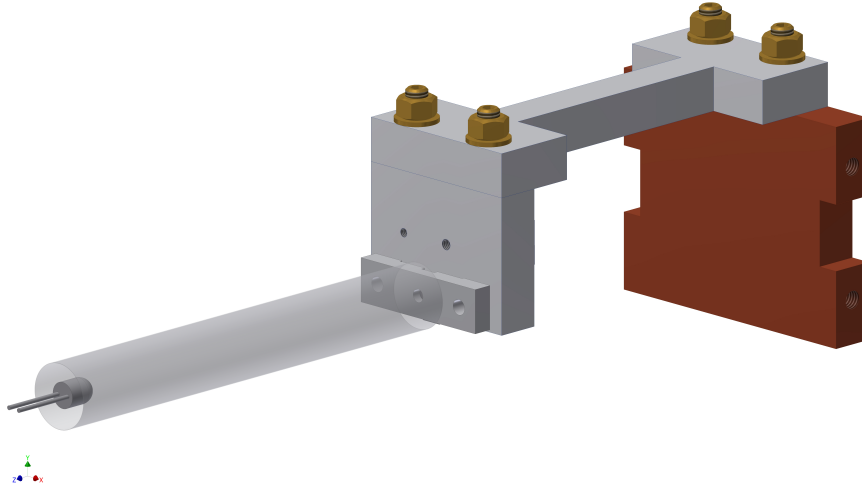


Figure 28: Set-up used for the low temperature behaviour of silicon photomultipliers. The copper block represents the cool tip. The detector is attached to the gray block made out of aluminium in the front. The long hollow cylinder is guiding the light (to avoid reflections at the wall of the DN160 cross) from the LED.

multipliers used. To make sure, that the light is guided to the SiPM and that no unnecessary reflection inside the cross will impinge the SiPM and falsify the results, a black long hollow paper cylinder with a diameter of 1.5 cm guides the LED-light all the way to the photon detector.

The LED was operated by a pulse generator. Pulsed light was used since a continuous beam of light would oversaturate the photon detector. Worth mentioning is that the signals produced by the SiPM were not independent of the frequency nor the width of the pulse produced by the pulse generator. A higher frequency resulted in a smaller amplitude of the signal, which is due to oversaturating of single pixels. Once a pixel fired it needs some time to recover to produce a signal again. Smaller pulse widths resulted in higher amplitudes. However, depending on the frequency and amplitude of the pulses there was a lower limit to the size of the pulse width, where no signal was produced anymore. A pulse width, which was too high, produced smaller and longer signals with a plateau in the middle (Fig. 29). A 5 V pulse with a 30 ns pulse width and 100 Hz frequency was used for the measurements. Those settings produced the most well-defined signal for the silicon photomultipliers used. It is estimated that around 100 photons are detected by the SiPMs at room temperatures. 100 mV signals were obtained which corresponds roughly to 100 photons.

In the following subchapters all three different SiPMs (3x3, 4x4, 6x6 mm²) are tested. Their waveforms at different temperatures are examined and changes compared. With the set-up shown in Fig. 28 the SiPM reached temperatures of 105 K. 105 K is close to the temperature achievable at the GRACE set-up with cooling (~ 100 K). However,

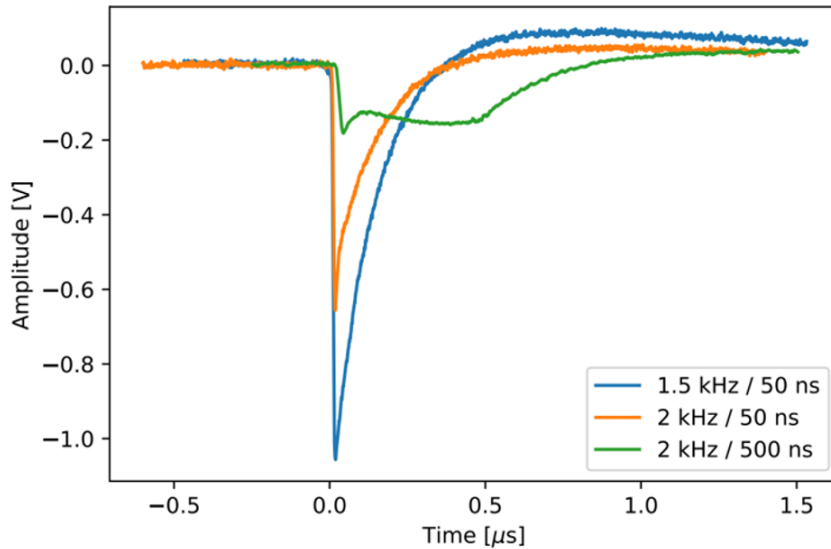


Figure 29: Dependence of the waveforms on frequency and pulse width. A higher frequency of the pulse produced smaller signals (blue/orange) and a pulse width set too high produced a long and small signal (green). For those waveforms the amplifier board (with an amplification of $V=3$) was used.

this is still too high for the final AEGIS experiment, where temperatures of 50 K have to be achieved. A final test at those low temperatures has still to be carried out. The signals were processed by the highpass boards without an amplifier. It was expected that changes in the waveforms might be altered by amplification. This way only the "pure" signals were examined and changes in properties of the SiPM are revealed.

6.2 Waveforms of Silicon Photomultipliers at low Temperatures

To examine the waveforms of a low temperature silicon photomultiplier is of great interest for the final set-up. By using a scintillator-independent set-up the "pure" waveforms can be analysed and by varying the temperature of the photon detector, changes in their efficiency can be observed. As stated above, all three different SiPMs (3×3 , 4×4 , 6×6 mm^2) were taken into consideration. Additionally of interest would be the low temperature behaviour of silicon grease or of optical glue. Those are sometimes used to enhance the coupling between the scintillators and the photon detectors. The worst case scenario would be that one of the components would freeze and therefore, decreases the coupling and the light transport. This subsection shows the results, starting with the silicon photomultiplier with an active area of 6×6 mm^2 .

6x6 mm²

As stated above the highpass board was used to process the signals. As a double check however, the signals processed by the amplifier were recorded as well. The variation of temperature was done by applying a current to the resistor. The lowest temperature reached at the SiPM's side with the refrigerant was 104 K. At 110 K however, the temperature fluctuation were less. So by already applying a current to the resistor, 110 K was used as starting temperature. The waveforms produced by the SiPM were recorded in 10 K steps all the way up to 230 K (a higher current and a higher temperature would have led to damage to the resistor and the set-up). The voltage was chosen so that a current of 2 μA would operate the SiPM while the LED was on. The pulse running the LED was kept at the same settings throughout the different measurements. The measurements were taken in a vacuum of $4.7 \cdot 10^{-7}$ mbar.

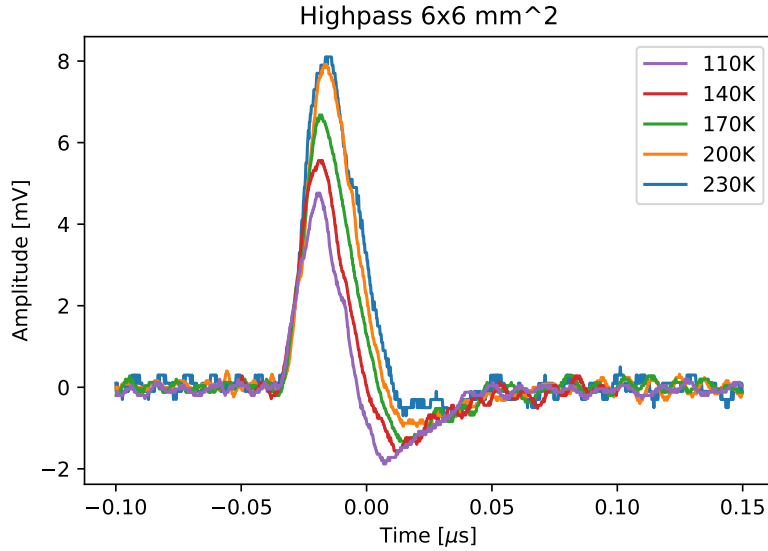


Figure 30: Changes in properties and functionality of a 6x6 mm² SiPM at different low temperatures. Signals were processed by the highpass board.

The signals of the SiPMs are shown in Fig. 30 for the highpass board and in Fig. 31 for the amplifier board. For the sake of clarity the waveforms are shown in 30 K steps. The figures show that the changes in temperature have similar effects. A lower temperature results in a smaller amplitude and a higher overshoot. The total length (including the overshoot) of the signal was not altered by change in temperature. The overshoot might be due to a change in capacity due to a change in permittivity of the SiPM's pixels. The change in impedance leads to a different coupling between the SiPM and the other parts of electronics and hence results in a light overshoot.

As discussed earlier an examination of property changes of silicon grease and optical glue would also be of interest for later experiments. To accomplish that, three new modifica-

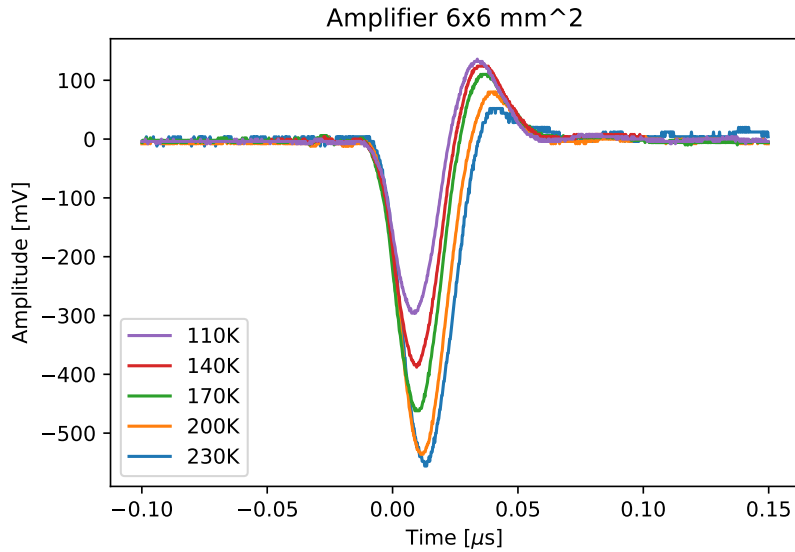


Figure 31: Changes in properties and functionality of a $6 \times 6 \text{ mm}^2$ SiPM at different low temperatures. The signals were processed by the amplifier.

tions were analysed. The first one was putting a piece of acrylic plastic ($6 \times 6 \times 2 \text{ mm}^3$) in front of the silicon photomultiplier (direct contact) and to again repeat the measurement done above. The plastic was large enough to cover the whole active area of the SiPM and fit inside the plastic cuboid seen in Fig. 28. The purpose of this intermediate step was to make sure that the plastic does not alter the results. The acrylic plastic was essential because a medium to glue on to the photon detector was needed to test the properties of the optical glue later on. The second and third changes to the set-up were to attach the acrylic plastic with optical grease (with detector and acrylic plastic still inside the plastic cuboid attached to the cool aluminium block by the screws) to the SiPM and later to glue it onto the SiPM with optical glue. The waveforms were then taken again with $2 \mu\text{A}$ applied to the SiPM at the temperatures of 110 K, 140 K, 170 K, 200 K and 230 K.

As can be seen in Fig. 32 no changes in waveforms can be observed for the different cases. In the interest of clarity the waveforms for the rest of the temperatures (110 K, 140 K, 200 K, 230 K) are not shown, since similar outcomes were obtained for those cases. Furthermore, no changes were observed while using the amplifier board to process the signals.

To summarize, the use of silicon grease nor the use of the optical glue alters the waveforms at low temperatures. This means that both will not absorb nor reflect any light from the LED at lower temperatures, which makes them possible candidates for scintillator-SiPM-coupling in future set-ups. The only changes were observed due to the change of permittivity at lower temperatures of the pixels of the SiPMs. Those changes however, were neglectable. The signals were still narrow and no slow component has appeared in

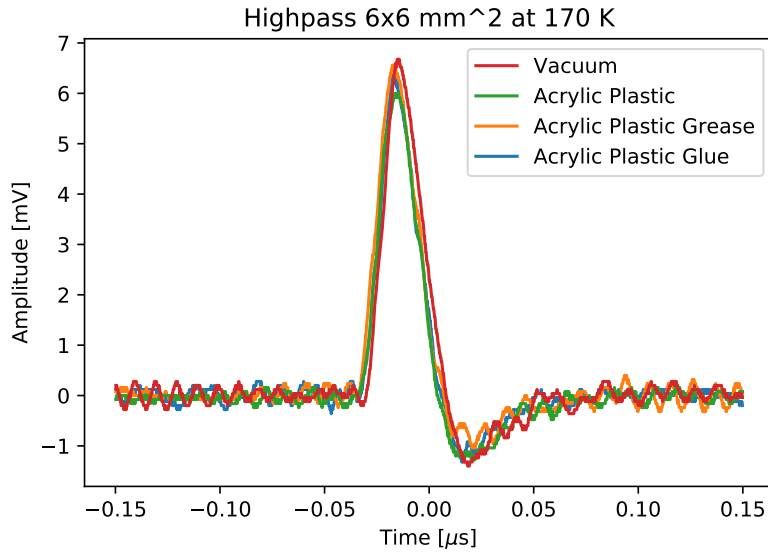


Figure 32: Comparison of vacuum, acrylic plastic, acrylic plastic with grease and acrylic plastic with optical glue in front of the $6 \times 6 \text{ mm}^2$ SiPM at 170 K. The signals were processed by the highpass board.

the SiPM's waveforms.

4x4 mm²

Changing the size of the plastic component (plastic cuboid) from Fig. 28, where previously the $6 \times 6 \text{ mm}^2$ detector fit, to a size that now fits the $4 \times 4 \text{ mm}^2$ silicon photomultiplier, made it possible to repeat the measurements shown above for the new smaller photon detector. The measurements with the acrylic plastic, the silicon grease and the optical glue were not repeated, since those measurements are independent of the silicon photomultiplier in use.

Again the same settings for the pulse generator were used. And the value of the voltage applied to the SiPMs was chosen so that $2 \mu\text{A}$ would operate the detector at different temperatures (110 K, 140 K, 170 K, 200 K, 230 K).

The corresponding waveforms can be seen in Fig. 33. This time the amplitudes of the signals were larger than for the $6 \times 6 \text{ mm}^2$ detector. This makes sense, since running a smaller photon detector with the same current results in higher amplitudes. The second difference to the previous subsection is that the overshoot of the waveforms does not change with decreasing temperature anymore. Apparently the $4 \times 4 \text{ mm}^2$ detector keeps a constant capacity even for lower temperatures. The last point worth mentioning is that the amplitudes of the signals were at first slightly increasing with lower temperatures. Around 170 K the amplitudes reached their maximum value of around 26 mV. Lower temperatures than 170 K however resulted in slightly smaller amplitudes again (23-24

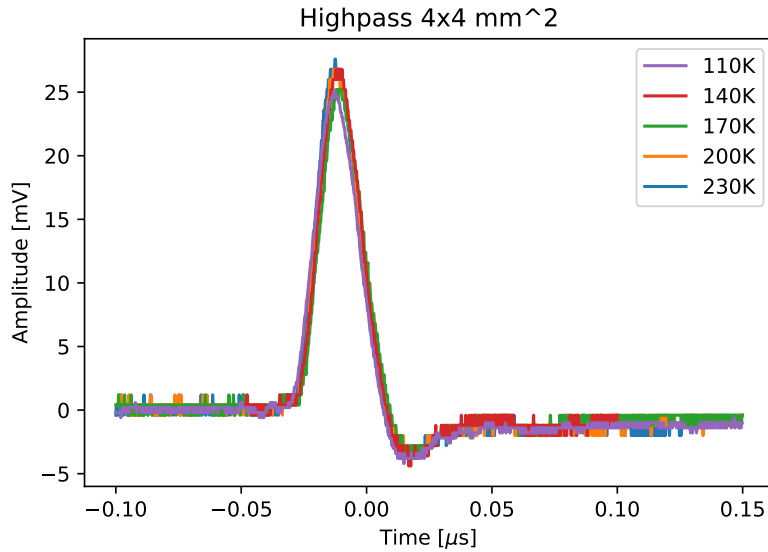


Figure 33: Changes in properties and functionality of a $4 \times 4 \text{ mm}^2$ SiPM at different low temperatures. The signals were processed by the highpass board.

mV). At higher temperatures thermal effects prevent some electron-hole pairs from contributing to the final signal (e.g. scattering with phonons). The cooling of the SiPM leads to a decrease in those thermal effects and therefore results in a higher amplitude of the signal (170 K). At even lower temperatures a freeze out of the electron-hole pairs occurs. This lower number of electron-hole pairs naturally produces a smaller signal [25].

$3 \times 3 \text{ mm}^2$

For the last set-up the plastic cuboid was exchanged once again for one component, that now fit the silicon photomultiplier with an active area of $3 \times 3 \text{ mm}^2$. Under the same conditions the measurements already done in the two previous subchapters were repeated. The results can be seen in Fig. 34. $2 \mu\text{A}$ again produced signals of higher amplitude. The overshoot did not change in size similar to the overshoot for the $4 \times 4 \text{ mm}^2$ detector. However, this time the behaviour of the first increasing and later decreasing amplitudes is more distinct. The largest amplitude was again reached at 170 K. Lower and higher temperatures result in signals of smaller amplitude.

With the help of a simple scintillator-independent set-up it was possible to examine the low temperature properties of three different commercially available silicon photomultipliers. Those measurements were crucial, since it is desirable for the final low temperature set-up to cool the SiPMs as well. The results showed that the behaviour of the low temperature SiPMs is acceptable for the final measurements. No slow component appeared in the waveforms of the SiPMs (as it does for example for the CsI). The

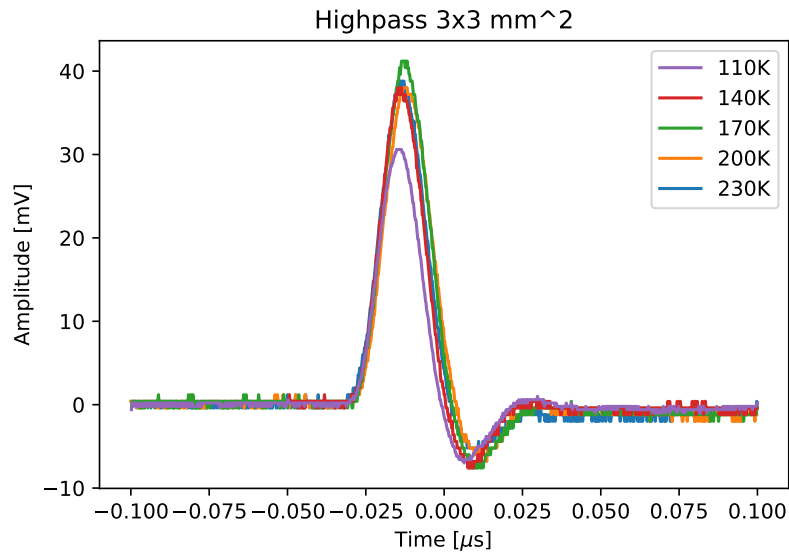


Figure 34: Changes in properties and functionality of a $3 \times 3 \text{ mm}^2$ SiPM at different low temperatures. The signals were processed by the highpass board.

electronics still work properly and produce well-defined, well-shaped signals. The low temperature behaviour of the SiPMs has been tested for several days and no change in properties occurred. Furthermore, no changes in the waveforms at low temperatures were seen while silicon grease or optical glue were used. The final set-up with a combined low temperature scintillator and silicon photonmultiplier are shown in the next chapter.

7 A cryogenic Caesium Iodide Detector for gravitational Measurements on Antihydrogen

After examining the low temperature behaviour of CsI and the silicon photomultipliers, it was essential to combine the two components to form a final set-up. SiPMs at low temperature showed no change in properties and produced well-defined signals. So attaching them with silicon grease or optical glue to the cryogenic CsI crystals should not result in any problems. The final set-up is shown and discussed in the next subsection.

7.1 A low Temperature Caesium Iodide Detector Set-up

It seemed natural to combine the two set-ups shown in Fig. 16 and in Fig. 28. The resulting final set-up can be seen in Fig. 35. The copper part again represents the cool tip. This time the aluminium bar connecting the front part with the cold-end was wider and longer (19 cm long and 6 cm wide). In comparison to the copper wires in Fig. 16 a better heat transfer was expected. The CsI crystals were again wrapped in aluminium and teflon with only the side facing the SiPMs free of it. Three CsI crystals were used and placed right next to each other in the hole of the aluminium block in the front. However in this set-up no gap was between the scintillators and the photon detectors. The SiPM on the left was glued to the CsI, the one in the middle connected via silicon grease and the third one was softly pressed against the third CsI (a screw in the back of the SiPM ensured the pressure, so they were in direct contact). A heat controller was added once again on the top of the aluminium bar. In this way spectra and waveforms at different temperatures can be examined again. The silicon photomultipliers used were single $6 \times 6 \text{ mm}^2$ photon detectors. Three Pt100 were added to the set-up. One attached to the cold-end, one on the top of the aluminium bar right next to the heat controller and the last one was in contact with the aluminium block itself. Heat paste between the cold-end and the bar, as well as between the bar and the block was used to increase the heat coupling.

On the opposite flange, where the LED used to be in the previous set-up (Fig. 28), a kapton window was attached once again. The radioactive ^{22}Na source is used again to produce signals. The aluminium bar was chosen to be longer than in the previous set-up, because it is desired to minimize the distance between the radioactive source and the scintillators. At a pressure of $2.3 \cdot 10^{-7}$ mbar the aluminium block reached temperatures of 105 K (lower temperatures than in chapter 4).

The measured spectra and waveforms are discussed in the next subsection.

7.2 Spectra and Waveforms of a low Temperature Caesium Iodide Detector

Spectra

The signals produced by the SiPMs were again fed into the ADC (again via the amplifier board V=3). A current of $1 \mu\text{A}$ was operating the SiPMs during the measurement.

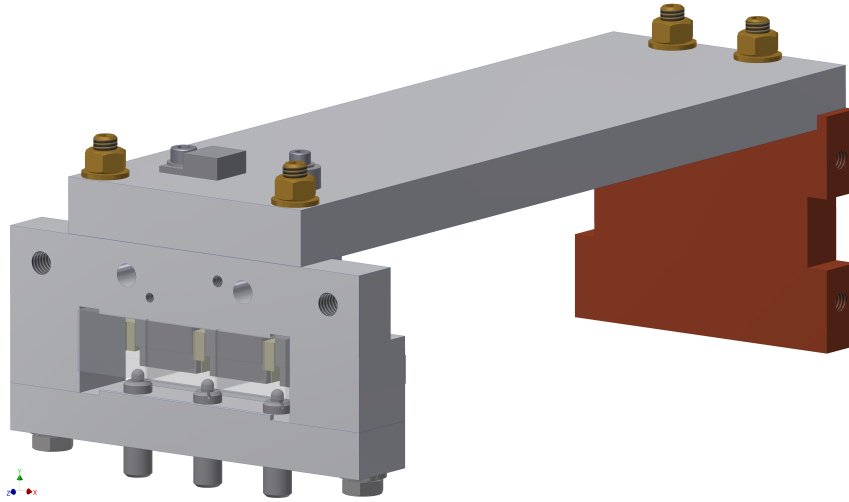


Figure 35: Set-up for a cryogenic CsI detector.

Before spectra were taken the signals and amplitudes were checked with the help of the oscilloscope. The count rate of the SiPM on the right (no glue, no grease) appeared lower than the one of the other two. This observation might be due to a weaker coupling between the SiPM and the scintillator and will be shown in the spectra. However the dark count rates of the photon detector on the right were 10% higher than the dark count rates of the other two (60000 counts in an hour versus 54000 counts for the other two). Fig. 36 shows three spectra for the three different silicon photomultipliers recorded over an 1 h time period. The spectra were recorded at a temperature of 105 K and a pressure of $2.5 \cdot 10^{-7}$ mbar.

From Fig. 36 it is easy to see that more light was incident onto the SiPM in direct contact with the CsI crystal. This did not result in a higher or lower count rate detected by the ADC (as seen on the oscilloscope), but in signals of bigger amplitudes. All three SiPMs were operated by the same current ($1 \mu\text{A}$). Since there is a wavelength shift for the CsI from a peak emission wavelength of 310 nm to 340 nm at lower temperatures, it is believed that the transmission of optical glue and silicon grease decreases at lower temperatures. This would explain why the signals' amplitudes were nearly twice as large for the SiPM in direct contact. This behaviour will later be observed again in the waveforms of the three different cases respectively. The number of counts after an hour of recording however was nearly the same for the three different cases (2774767 counts direct contact / 2832326 counts glue / 2639737 counts silicon grease).

In Fig. 37 the energy calibrated spectra from Fig. 36 are shown. The calibration was carried out with the MC²-Analyzer-software to identify the energy resolution of the three different SiPMs. To do so the FWHM was calculated for all six peaks respectively (three 511 keV peaks and three 1275 keV peaks). In addition, the number of counts between the FWHM values were integrated. This helps to characterize and distinguish the different cases even more. The corresponding results can be seen in Tab. 3.

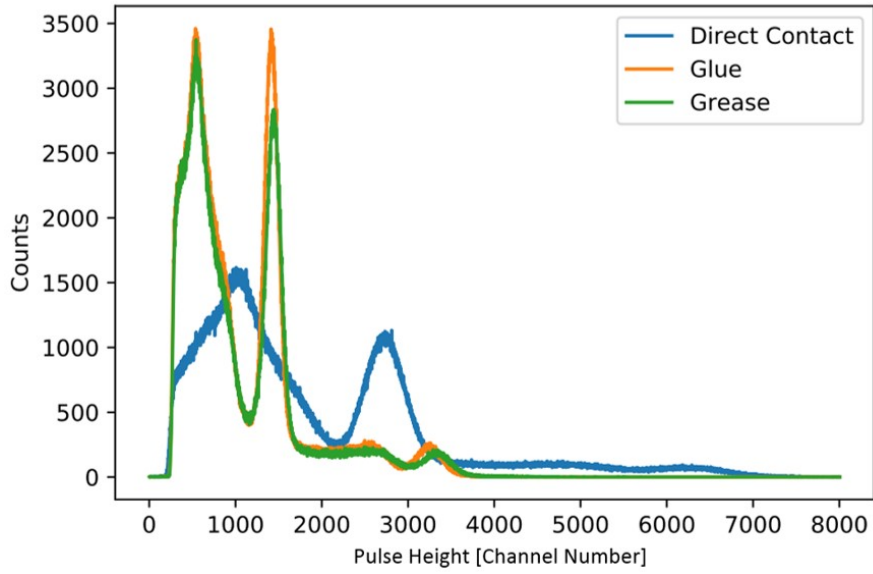


Figure 36: Spectra recorded for the three different SiPMs (1 h measuring time, 105 K, $2.5 \cdot 10^{-7}$ mbar).

The results from Tab. 3 underline the outcome shown in Fig. 37. The peaks with the best energy resolution containing the biggest number of counts were produced by the SiPM connected to the scintillator with optical glue. While the silicon grease's results were satisfying as well and close to the ones of the optical glue, the results of the SiPM in direct contact with the CsI crystal were not. The energy resolution for this case was worse by nearly 50% for the 511 keV peak.

After taking first measurements and spectra the temperature was increased with the

Table 3: Energy Resolution and Counts for the Spectra shown in Fig. 37

Direct Contact		
	$\Delta E(\text{FWHM})$ [keV]	Counts
511 keV	120	497 960
1275 keV	192	59 173
Glue		
511 keV	82	544 868
1275 keV	131	61 873
Silicon Grease		
511 keV	86	483 549
1275 keV	143	55 368

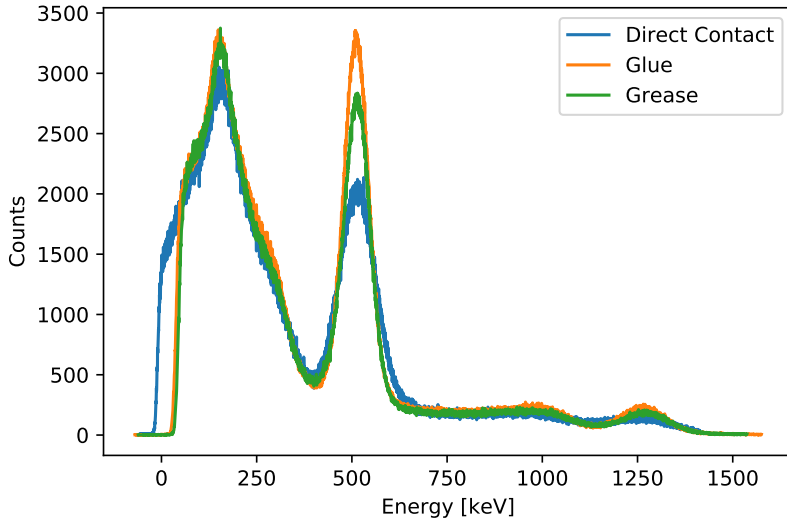


Figure 37: Energy calibrated spectra recorded for the three different SiPMs (1 h measuring time, 105 K, $2.5 \cdot 10^{-7}$ mbar).

help of the temperature controller. The temperature range that allowed to see a decent spectrum was of particular interest. Additionally, the change in count rates was monitored. Spectra were taken at 140 K, 170 K, 200 K and 230 K. A current of $1 \mu\text{A}$ was set to operate the SiPMs at all temperatures.

At 170 K it was still possible to identify both ^{22}Na peaks (511 keV and 1275 keV) for all three CsI crystals. At 200 K for the SiPM in direct contact with the CsI however, the count rate decreased significantly and the 1275 keV peak vanished (not shown for the sake of clarity). For the other two SiPMs the 1275 keV peak at 200 K was still resolvable (not shown). The spectra for the optical glue were similar to Fig. 39 and are not shown here. Worth mentioning is, that for the SiPMs connected to the scintillators with optical glue and silicon grease a similar behaviour to the behaviour of the 3×3 and 4×4 mm² at low temperatures was observed. At 170 K the amplitudes of the signal increased, while they were smaller for higher and lower temperatures.

Furthermore, five one day long spectra were recorded for the SiPM glued to the scintillator. The purpose of those measurements was to check if a drift in the spectra would appear (peaks at different positions in the spectra). This might happen due to a change in current applied to the SiPM or a change in properties of the SiPM. However, the five spectra were identical, showing that the measurements were reproducible and that the current was stable.

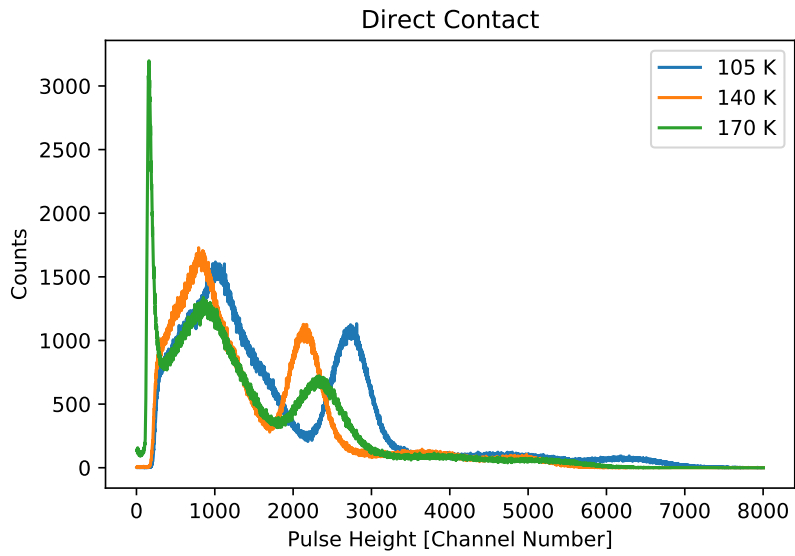


Figure 38: Spectra recorded at different temperatures for the SiPM in direct contact with the CsI (1 h).

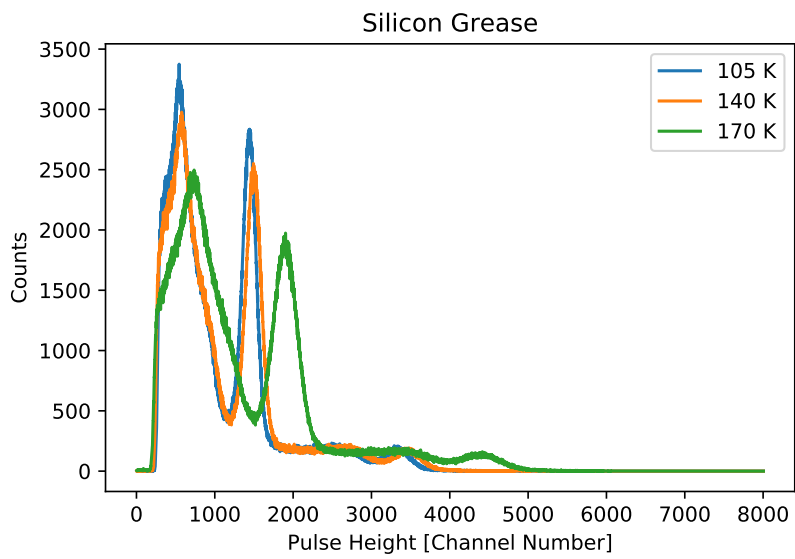


Figure 39: Spectra recorded at different temperatures for the SiPM with silicon grease (1 h).

Waveforms

Similar to the previous chapter waveforms were recorded at the different temperatures using the highpass board and the amplifier board II. At low temperatures the signals again were too long (due to the slow component of the CsI) for the amplifier board II to work properly. A higher current was needed ($8 \mu\text{A}$ at 105 K for example) to produce a signal. However the shape of those signals was questionable and not of use for the comparison at different temperatures. So in the following, only the waveforms from the highpass board are examined. A current of $1 \mu\text{A}$ was operating the SiPMs throughout the measurements.

Fig. 40 to 42 show the waveforms of the three different SiPMs. The waveforms are not averaged over a larger sample, they are merely snapshots. Small fluctuations in amplitudes might occur, which do not change or alter the outcome significantly.

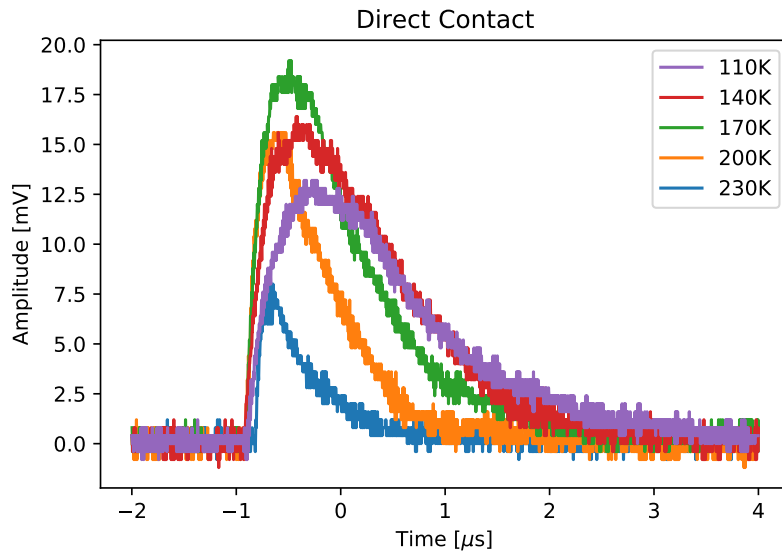


Figure 40: Signals produced by the SiPM ($6 \times 6 \text{ mm}^2$) in direct contact with the scintillator.

All three silicon photomultipliers showed similar behaviour. At low temperatures longer signals than at higher temperatures were detected (slow component of the scintillator). At 170 K to 200 K an amplitude maximum was detected. This makes sense since the signals do get shorter but the light yield does not decrease that fast. At even higher temperatures even shorter signals appeared, now with a smaller amplitude due to the decrease in light yield. The signals at the different temperatures were roughly all of the same amplitude. However, for the SiPM in direct contact with the scintillator the amplitudes differed from the other two SiPMs. The signals at lower temperatures were larger (similar to the spectra) but smaller at 230 K (weaker coupling). The behaviour of the SiPM with silicon grease and the SiPM with optical glue were nearly identical. It is

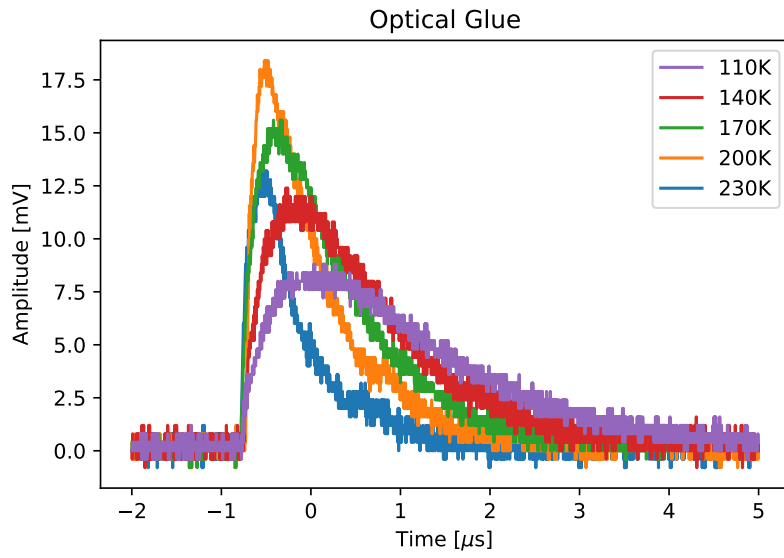


Figure 41: Signals produced by the SiPM ($6 \times 6 \text{ mm}^2$) connected to the scintillator with optical glue.

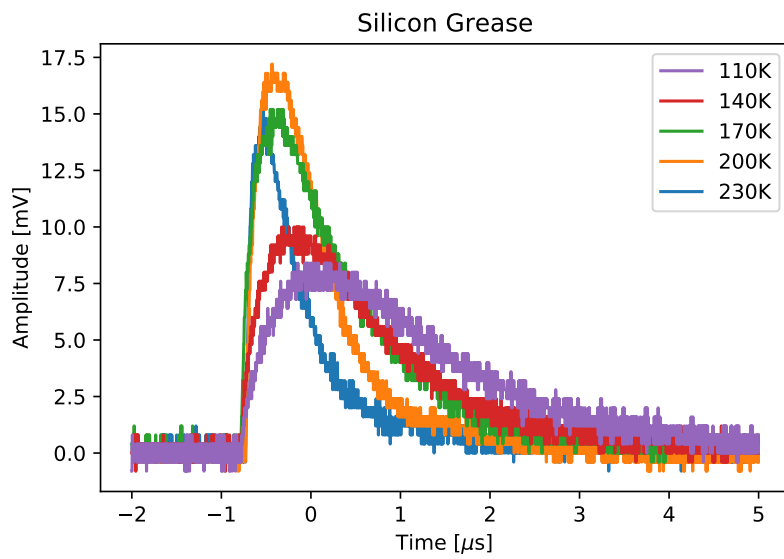


Figure 42: Signals produced by the SiPM ($6 \times 6 \text{ mm}^2$) connected to the scintillator with silicon grease.

worth mentioning, that the difference in amplitudes for the three different cases at 105 K, was approximately the same difference as the difference in the spectra. Meaning that the amplitude for the SiPM with grease and optical glue at 105 K is roughly 7.5 mV and the amplitude for the direct contact case is 12.5 mV, approximately the same ratio holds for peaks and the corresponding channel numbers in Fig. 36 (1500 for glue and grease and 2800 for direct contact).

The combined low temperature CsI crystals and SiPMs performed well. By looking at the low temperature behaviour of both components individually in the previous chapters, it was easy to interpret the results. The set-up shown above perfectly demonstrated the freeze out of the fast component and the increase in light yield of a CsI-scintillator at lower temperatures. The spectra recorded by the detector system were of a high resolution. Additionally the coupling with glue and grease seemed to be better than by just putting both components in contact. In addition with all three connections being suitable candidates, optical glue might be the simplest, since no extra mounting for the SiPMs would be needed. The next section discusses a first test for this detector at the GRACE line at CERN.

8 Final Test of the cryogenic Caesium Iodide Detector

8.1 Set-up for the final Test at the GRACE Beam line at CERN

The GRACE beam line at CERN is located at the AD, the antiproton decelerator, right next to the AEGIS set-up [20]. The GRACE line's main purpose is the extraction of very low energy antiprotons from the CERN AD. During one shot approximately $3 \cdot 10^7$ antiprotons with energies of 5.3 MeV cycle inside of the AD. The GRACE line is one arm of the AD and consists of a long set of degrader foils and magnets, which slow down and guide the antiprotons to the end of this line. Here a flange for the test of different detectors can be attached.

The final set-up for the test can be seen in Fig. 43. It represents a compact modification of the set-up shown in Fig. 35. Again three CsI crystals ($17 \times 17 \times 13 \text{ mm}^3$) were used, this time however the sides facing the antiproton beam (front side) were free of foil and teflon. All three SiPMs were now glued onto the scintillators. The aluminium block holding them was the same as in Fig. 35. The back of the block was attached to the flange via an aluminium connector. Here one Pt100 was placed right behind the crystals to monitor the temperature.

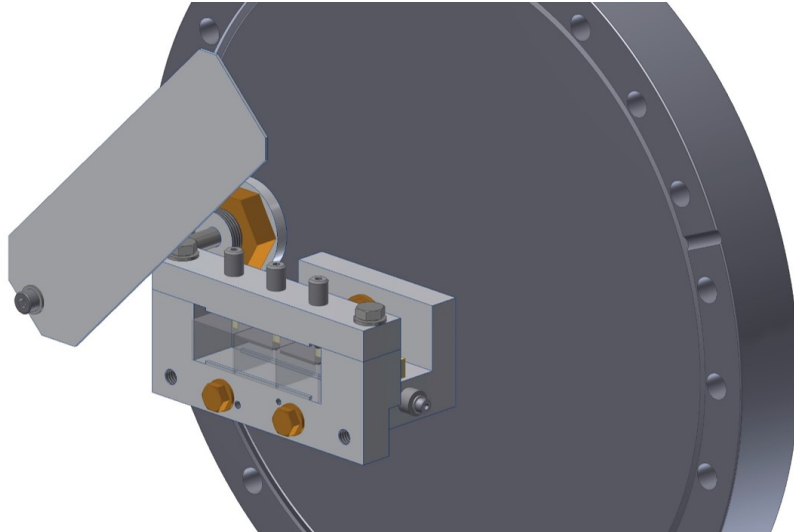


Figure 43: Final set-up for the last test at the GRACE line.

To process the signals three identical highpass boards shown in Fig. 7 were used. Before the signals were fed into a four-channel oscilloscope (LeCroy, WAVEPRO7K), they passed through an amplifier (LeCroy, Model: 612AM, six channel variable amplifier). For larger signals the module does not work for positive amplitudes, so the biasing voltage at the highpass boards was simply reversed (signals appear negative now).

The major differences were the connection to the LN_2 (liquid nitrogen) cooling and the rotatable aluminum shield shown in the left of Fig. 43. Antiprotons were stopped by the shield of a thickness of 1 mm by rotating it in front of the CsI crystals. The

stopped antiprotons annihilate. Pions produced in these annihilation processes however, are not stopped by the shield. Comparing signals with and without the shield blocking antiprotons, makes it possible to identify the signals produced by antiprotons directly in the CsI or aluminium shield, respectively. The outside of the flange was formed like a funnel. By pouring liquid nitrogen into the funnel (filling capacity of around two liters), it was possible to cool the detector set-up. Covering the opening of the funnel with aluminium foil kept the set-up at low temperatures throughout the total beam time.

8.2 Identification of antiproton annihilation signals

At first the set-up was tested at room temperature at a pressure of $2.8 \cdot 10^{-7}$ mbar, $2 \mu\text{A}$ operating the SiPMs with. A trigger signal from the AD made it easy to record the waveforms of an antiproton shot on the oscilloscope. One antiproton shot recorded with one of the SiPMs can be seen in Fig. 44.

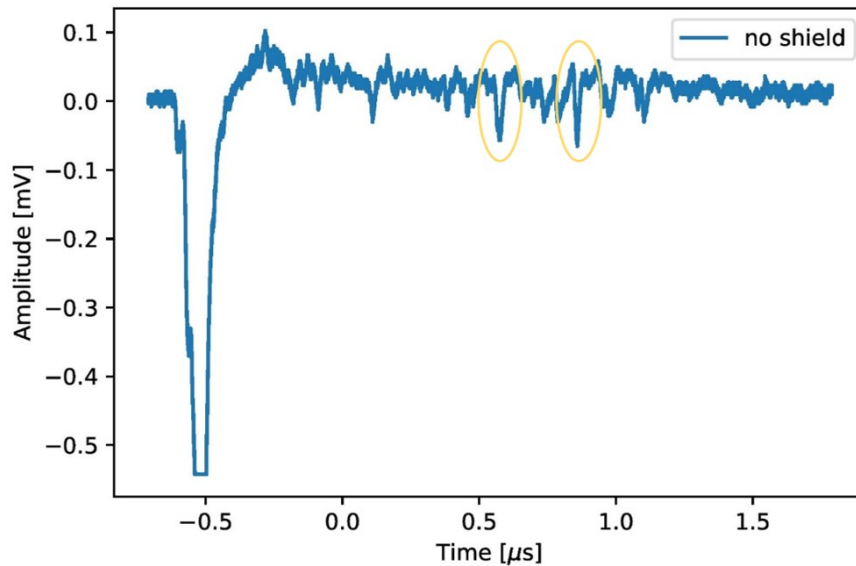


Figure 44: Antiproton shot recorded with one of the detectors at room temperature. No aluminum shield was in front of the scintillators.

The large peak in the left of the figure corresponds to antiprotons, which annihilated upstream in the degrader foils. In those annihilation processes a multitude of fast pions are produced and some of them are detected by the SiPMs. The slower heavier antiprotons arrive later, probably two of them (larger peaks) can be seen between 0.5 and 1.0 μs (orange circles). Per shot between one and three peaks were identified as antiprotons. In comparison, Fig. 45 shows one shot with the shield in front of the CsI crystals (orange) and one without it (blue). There was an offset in amplitude (± 0.5 mV) added to both waveforms for the sake of clarity.

Smaller peaks are due to detected pions. So by rotating the shield in and out, it was

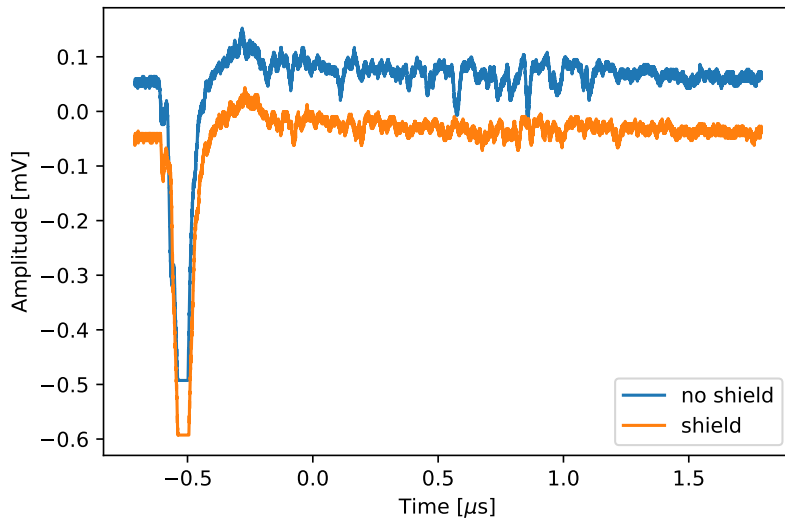


Figure 45: Antiproton shot recorded with one of the detectors at room temperature. With (orange) and without (blue) the aluminium shield in front of the scintillators.

possible to identify clear antiproton signals.

There were difficulties with the low temperature measurement, which causes are not well understood yet. Due to ongoing data analysis at the time of completion of this thesis, there are no definitive results to be shown.

The next chapter gives a summary and an outlook on the future developments to this detector.

9 Discussion and Outlook

This diploma thesis has been carried out to present a possible detector candidate for the measurement of the sign of the gravitational acceleration of antihydrogen (30% relative precision) at the AEGIS experiment at CERN.

The work demonstrates, that by testing different light guides, where optical fibers proved to be an interesting alternative worth investing into, a suitable set-up for the detector was found. The set-up allowed a characterization of the low temperature behaviour of the Caesium Iodide crystals, while the silicon photomultipliers were kept at room temperatures. It was possible to take a good quality decay spectrum of a radioactive ^{22}Na source. The signals of the cold CsIs showed the well known decrease in their fast component, with only producing long decay time signals at cryogenic temperatures.

While being aware of this behaviour, a comparison of CsI and LYSO crystals was carried out. Since no slow component at low temperatures was observed for the LYSO crystals, they confirmed to be a promising candidate for the final detector.

For a future combined cryogenic CsI-SiPM detector, it was essential to examine the low temperature properties of the SiPMs individually. This was done with a separate scintillator-independent set-up. Since no big changes in the SiPMs waveforms have been found for different low temperatures, the way was clear for a combined detector.

In the final combined cryogenic set-up the best connection between the scintillators and the silicon photomultipliers was found to be optical glue. It was again possible to take spectra of high quality of the radioactive ^{22}Na source and to examine signals and waveforms at different temperatures. The results were satisfying and the detector ready for the last final test at the GRACE beam line at CERN.

While the first quick analysis of the room temperature measurements taken at CERN was satisfying, a more elaborated analysis is still ongoing.

The CsI proved to be a fast detector at room temperature. At cryogenic temperatures the difficulties due to a longer decay time in measurements at the GRACE line are known. For the final antihydrogen measurement however, this behaviour should not cause any problems.

The unexpected difficulties, which appeared during the low temperature test at the GRACE line, need to be understood and solved. For the final set-up test, a comparison with LYSOs, as a promising alternative to the CsI, should be done. Furthermore the behaviour of the set-up and its individual components at even lower temperatures (~ 50 K) should be investigated, since those temperatures will be crucial for the final AEGIS set-up.

Appendix: Datasheets of the Silicon Photomultipliers



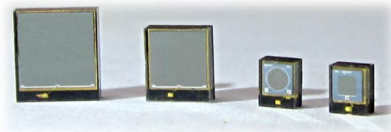
NUV SiPMs Chip Scale Package (CSP)

NUV SiPMs

The Silicon PhotoMultiplier (SiPM) is an innovative solid-state silicon detector with single photon sensitivity. SiPMs are a valid alternative to photomultiplier tubes (PMT detectors). The main benefits of this detector are: high gain, extremely good timing performance, low operative voltage, insensitivity to magnetic field and high integration level.

ASD-NUV SiPMs are based on the AdvanSiD "P-on-N" silicon technology for detection of Near Ultraviolet Light. NUV-SiPMs have peak efficiency at 420nm, with detection spectrum extending from 350nm to 900nm.

Chip Scale Package (CSP) plastic SMD package provides a cost-effective solution to achieve greater board density and high performances.



Features

- Near Ultra Violet light detection
- Low noise
- Afterpulsing probability < 4 %
- Dark Count Rate < 100 kHz/mm²
- Superior breakdown voltage uniformity
- Excellent temperature stability
- Detection of extremely faint light
- Very high gain (10⁶)
- Extremely good timing performance
- Insensitive to magnetic fields
- Not damaged by ambient light
- Small and compact
- CSP Nickel free

Application

- High Energy Physics
- Medical Imaging
- Nuclear Medicine
- DNA Sequencing
- Homeland Security
- Flow Cytometry
- Biological Sensors
- Analytical Instruments
- SEM Microscopy
- Confocal Microscopy

Ordering Information

Product Code	Description
ASD-NUV1S-P	1x1 mm ² active area SiPM
ASD-NUV1C-P	1.2 mm diameter circular active area SiPM
ASD-NUV3S-P	3x3 mm ² active area SiPM
ASD-NUV4S-P	4x4 mm ² active area SiPM

S indicates square SiPM; C indicates circular SiPM; P indicates plastic chip scale package (CSP).

NUV SiPMs

Absolute Maximum Ratings

Symbol	Parameter	Min	Max	Unit
T _A	Operating Temperature Range	-25	+40	°C
T _s	Storage temperature	-40	+60	°C
T _{sol}	Lead temperature (solder) 5s		+250	°C
M _{VW}	Max voltage working range	Breakdown Voltage + 6		V

Stresses beyond those listed under "Absolute Maximum Ratings" may cause permanent damage to the device. These are stress ratings only, and functional operation of the device at these or any other conditions beyond those indicated in the operational sections of the specifications is not implied. Exposure to absolute maximum rated conditions for extended periods may affect device reliability.

Geometrical, Electrical, and Optical Typical Characteristics (T_a = 20 °C)

Symbol	Parameter	Product			
		ASD-NUV1S-P	ASD-NUV1C-P	ASD-NUV3S-P	ASD-NUV4S-P
AA	Effective active area	1x1 mm ²	1.13 mm ²	3x3 mm ²	4x4 mm ²
N	Cell count	625	673	5520	9340
CS	Cell size (pitch)	40 μm x 40 μm			
FF	Cell fill-factor	60 %			
RQ	Quenching resistance	800 kΩ			
C	Cell capacitance	90 fF			
τ _{RC}	Recharge time constant	70 ns			
S _R	Spectral response range	350 to 900 nm			
λ _p	Peak sensitivity wavelength	420 nm			
PDE	Photon Detection Efficiency ⁽¹⁾	43 %			
BV	Breakdown voltage ⁽²⁾	Typical: 26 V	Min: 24 V	Max: 28 V	
σ _{BV}	BV standard deviation ⁽³⁾	50 mV			
OV	Recommended Overvoltage range ⁽⁴⁾	Min: 2 V		Max: 6 V	
DCR	Dark Count Rate ⁽⁵⁾	< 50 kHz/mm ² @ 2 V OV		< 100 kHz/mm ² @ 6 V OV	
G	Gain ⁽⁶⁾	3.6x10 ⁶			
BVTC	Breakdown Voltage Temperature Coefficient	26 mV/°C			
n _{epoxy}	Refractive index of epoxy resin ⁽⁷⁾	1.5115 (@ 589 nm, 23°C, uncured)			
T _{epoxy}	Spectral transmission of epoxy resin ⁽⁷⁾	> 97% @ 1000 – 1600 nm ; > 99% @ 400 – 1000 nm			

- (1) Measured at peak sensitivity wavelength (λ = λ_p) at +6 V overvoltage (not including afterpulse and crosstalk).
- (2) Refer to the data provided with each shipped product.
- (3) BV of SiPMs belonging to a same production lot is within 200 mV (±2σ) from mean BV value.
- (4) Operating voltage (SiPM bias) is BV + OV, to be applied in reverse mode, i.e., V_{AK} < 0 (see "Pins Function" section).
- (5) 0.5 p.e. threshold level at 20 °C (primary dark count rate; not including afterpulse).
- (6) Measured at 20 °C at +6 V overvoltage.
- (7) To be used as a guide only, not as a specification. Reported data is not guaranteed.

Information in this datasheet is believed to be reliable. However, no responsibility is assumed for possible inaccuracies or omissions. Specification are subject to change without notice.

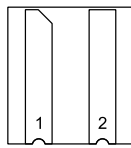
NUV SiPMs

Dimensional Outlines

Units = mm, Mechanical tolerance = ± 0.15 mm unless otherwise noted.

Product	Top View	Side View	Bottom View
ASD-NUV1S-P SMD package for SiPM 1x1 mm ² active area size Material: Black FR4 + transparent epoxy layer			
ASD-NUV1C-P SMD package for SiPM 1.2 mm circular active area size Material: Black FR4 + transparent epoxy layer			
ASD-NUV3S-P SMD package for SiPM 3x3 mm ² active area size Material: Black FR4 + transparent epoxy layer SLIM PACKAGE			
ASD-NUV4S-P SMD package for SiPM 4x4 mm ² active area size Material: Black FR4 + transparent epoxy layer SLIM PACKAGE			

Pins function



CSP bottom view



N°	Name	Function
1	K	SiPM Cathode
2	A	SiPM Anode

NUV SiPMs

Device Characteristics

This section reports typical SiPM reverse and forward I/V curves and the dependences on overvoltage, temperature, and wavelength of most relevant device parameters. Refer to the data accompanying each shipped product for more detailed information.

All measurements are performed in a tight-light climatic chamber at $T=20^{\circ}\text{C}$, unless otherwise noted.

SiPM output signals are amplified with ASD-EP-EB-N or ASD-EP-EB-PZ evaluation boards and acquired with fast oscilloscopes; the digitized data is then processed with dedicated PC programs.

Explanation of SiPM working principle and details on SiPM properties parameters can be found on the *Introduction to SiPMs* available at <http://advansid.com/resources/the-silicon-photmultiplier>.

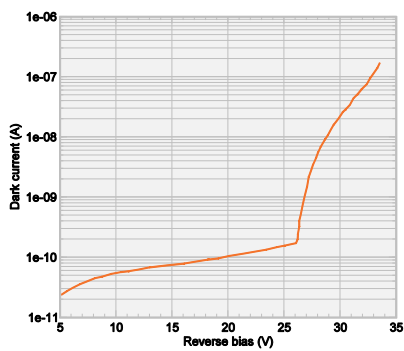


Fig.1 Typical reverse IV curve (ASD-NUV1S-P).

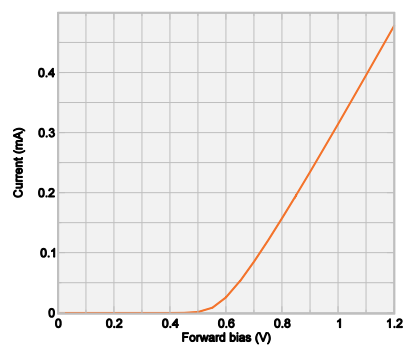


Fig.2 Typical forward IV curve (ASD-NUV1S-P).

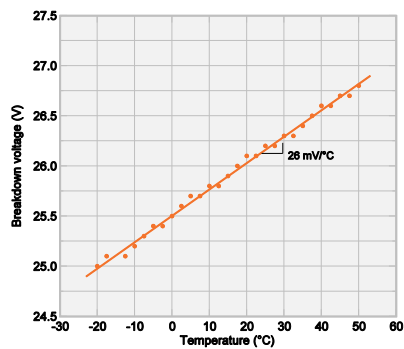


Fig.3 NUV-SiPMs breakdown voltage temperature dependence.

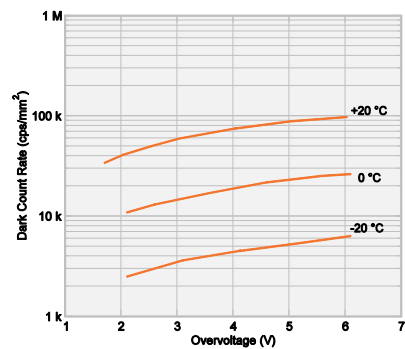


Fig.4 Dark count rate per square mm in NUV-SiPMs as a function of overvoltage and temperature.

NUV SiPMs

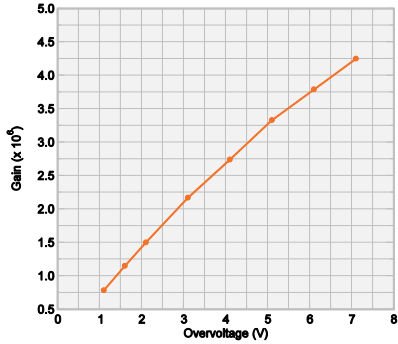


Fig.5 Gain of NUV-SiPMs as a function of overvoltage.

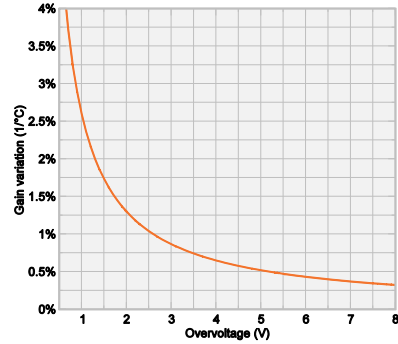


Fig.6 Relative variation of gain with temperature in NUV-SiPMs as a function of overvoltage.

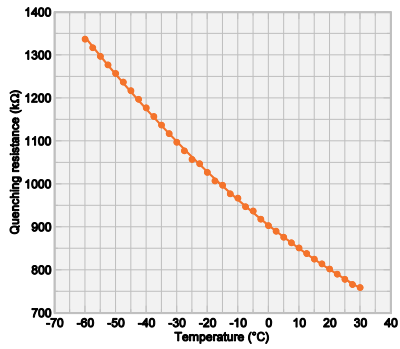


Fig.7 Temperature dependence of poly-silicon quenching resistance in NUV-SiPMs.

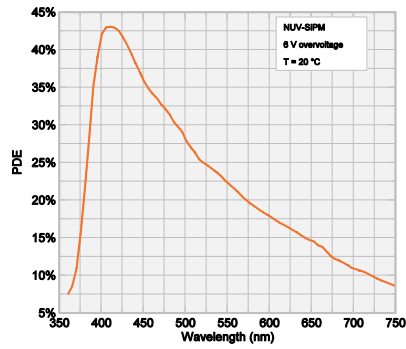


Fig.8 Photo detection efficiency (PDE) in NUV-SiPMs as a function of wavelength (crosstalk and afterpulse not included).

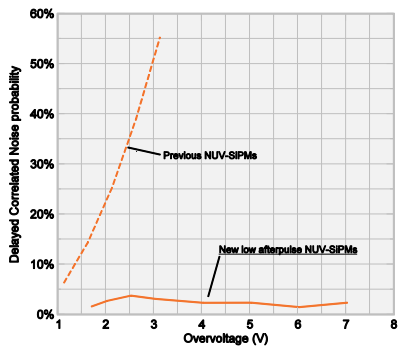


Fig.9 Delayed correlated noise probability (delayed crosstalk and afterpulse) in NUV-SiPMs.

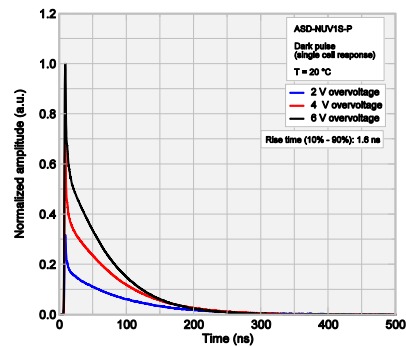


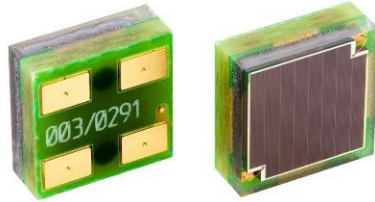
Fig.10 NUV-SiPM pulse shape (dark pulses, single cell response) at different overvoltage. Recharge time constant is 70 ns. Signals acquired with ASD-EP-EB-N.



Product Data Sheet

SiPM – Silicon Photomultiplier

PM3325-EB / PM3350-EB



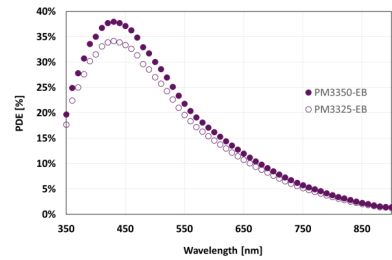
PM33 Series in new Chip Size Package

Key Features Overview

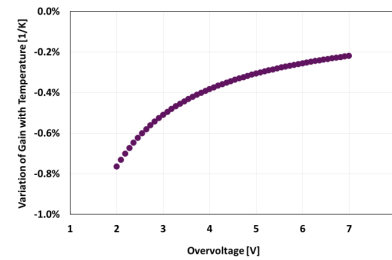
- High Photo Detection Efficiency
- Excellent Timing Properties
- Extremely low Temperature Coefficient
- New Chip Size Package suitable for Arrays
- MSL1 approved

1. SiPM Key Features

Absolute Photo Detection Efficiency at 5 V overvoltage



Temperature Dependency of the Gain



2. SiPM General Parameters

General Parameters					
Type	Active Area [mm ²]	Microcell Size [μm]	No. of Microcells	Package Dimensions [mm ³]	Order-Code
PM33	3.0 x 3.0	25	13408	3.50 x 3.50 x 1.45	PM3325-EB
		50	3472		PM3350-EB

3. Main Characteristics

Main Characteristics		
Parameter	Typ.	Unit
Breakdown Voltage (V _{BD})	25.0	V
Recommended Overvoltage (V _{OV})	2.0 – 7.0	V
Temperature Dependency of V _{BD}	18.0	mV/K
Temperature Dependency of Gain	0.3% @ 5.0 V _{OV}	1/K

KETEK GmbH
 Hofer Str. 3
 81737 Munich, Germany
 www.ketek.net
 info@ketek.net
 phone +49 89 673 467 70
 fax +49 89 673 467 77





Product Data Sheet

SiPM – Silicon Photomultiplier

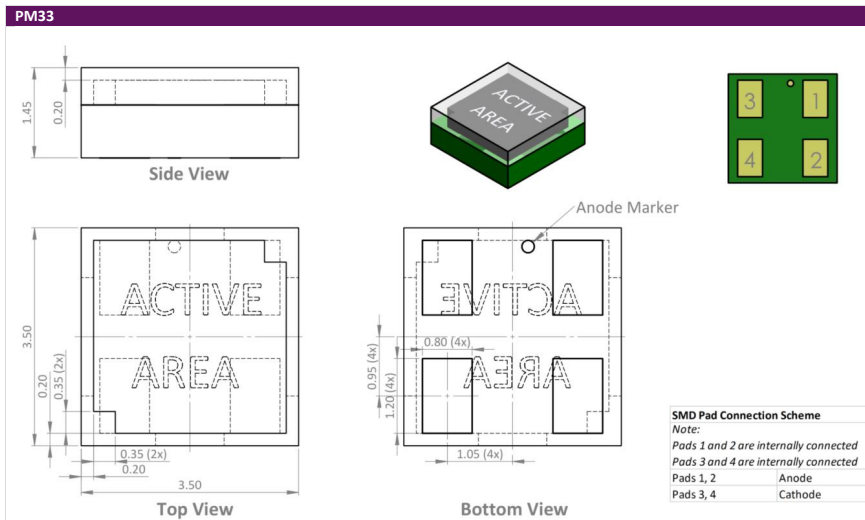
PM3325-EB / PM3350-EB



4. Performance Overview

Performance Overview					
Parameter	Type	Microcell Size [μm]	Typ. @ 2.5 V _{ov}	Typ. @ 5.0 V _{ov}	Unit
Photo Detection Efficiency @ 430 nm	PM33	25	26	34	%
		50	28	38	
Dark Count Rate	PM33	25	250	500	kHz/mm ²
		50	250	500	
Crosstalk Probability	PM33	25	10	30	%
		50	10	25	
Afterpulse Probability	PM33	25	1	3	%
		50	1	3	
Gain	PM33	25	0.9	1.7	x 10 ⁶
		50	3.6	7.2	
Terminal Capacitance	PM33	25	790		pF
		50	810		
Recovery Time τ	PM33	25	35		ns
		50	130		
Signal Rise Time	PM33	25	< 1		ns
		50	< 1		

5. Technical Drawing and Footprint



KETEK GmbH
 Hofer Str. 3
 81737 Munich, Germany
 www.ketek.net
 info@ketek.net
 phone +49 89 673 467 70
 fax +49 89 673 467 77

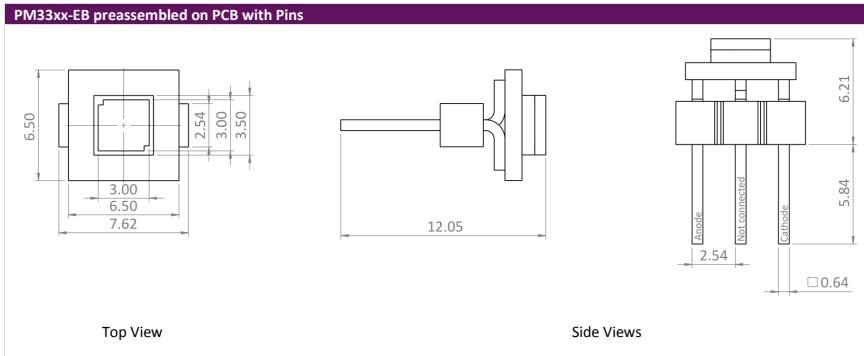




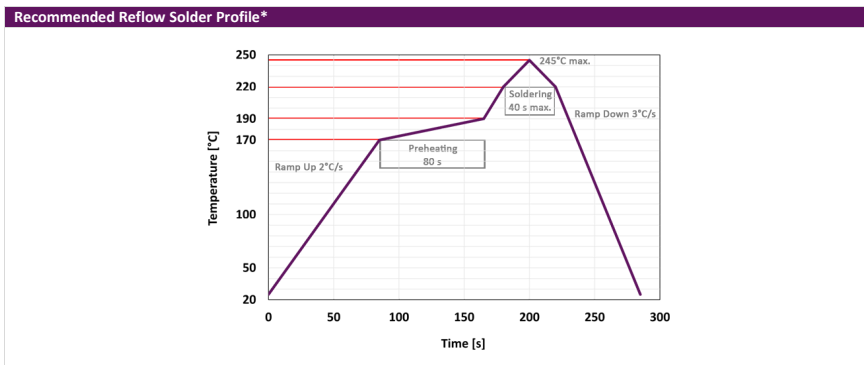
Product Data Sheet
SiPM – Silicon Photomultiplier
PM3325-EB / PM3350-EB



6. Pin Variant



7. Reflow Solder Profile



* Soldering under nitrogen atmosphere is recommended to avoid deterioration of the highly transparent epoxy encapsulation

KETEK GmbH
 Hofer Str. 3
 81737 Munich, Germany
 www.ketek.net
 info@ketek.net
 phone +49 89 673 467 70
 fax +49 89 673 467 77

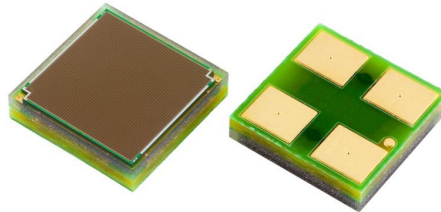




Product Data Sheet

SiPM – Silicon Photomultiplier

PM6625-EB / PM6650-EB



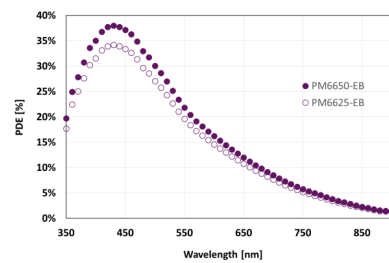
PM66 Series in new Chip Size Package

Key Features Overview

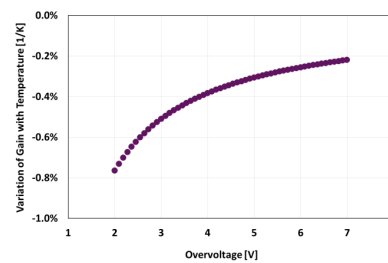
- High Photo Detection Efficiency
- Large Active Area
- Extremely low Temperature Coefficient
- New Chip Size Package suitable for Arrays
- MSL1 approved

1. SiPM Key Features

Absolute Photo Detection Efficiency at 5 V overvoltage



Temperature Dependency of the Gain



2. SiPM General Parameters

General Parameters					
Type	Active Area [mm ²]	Microcell Size [μm]	No. of Microcells	Package Dimensions [mm ³]	Order-Code
PM66	6.0 x 6.0	25	55168	6.50 x 6.50 x 1.45	PM6625-EB
		50	14272		PM6650-EB

3. Main Characteristics

Main Characteristics		
Parameter	Typ.	Unit
Breakdown Voltage (V _{BD})	26.5	V
Recommended Overvoltage (V _{OV})	2.0 – 5.0	V
Temperature Dependency of V _{BD}	18.0	mV/K
Temperature Dependency of Gain	0.3% @ 5.0 V _{OV}	1/K

KETEK GmbH
 Hofer Str. 3
 81737 Munich, Germany
 www.ketek.net
 info@ketek.net
 phone +49 89 673 467 70
 fax +49 89 673 467 77





Product Data Sheet

SiPM – Silicon Photomultiplier

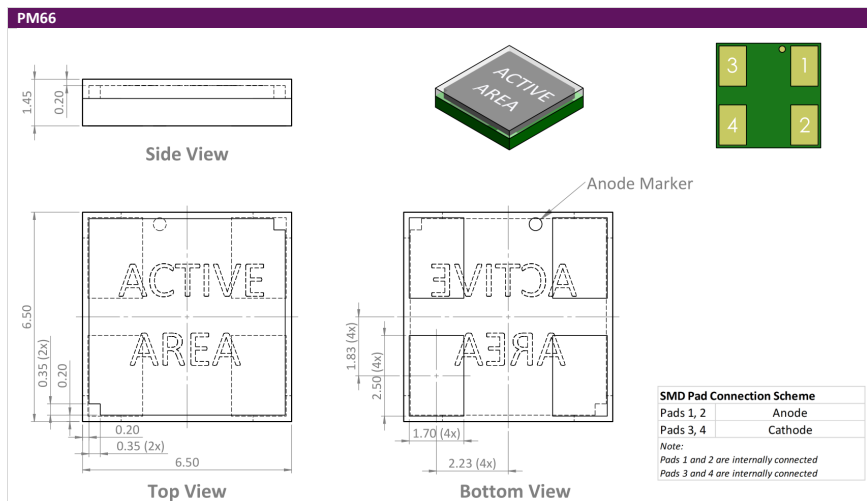
PM6625-EB / PM6650-EB



4. Performance Overview

Performance Overview					
Parameter	Type	Microcell Size [μm]	Typ. @ 2.5 V _{OV}	Typ. @ 5.0 V _{OV}	Unit
Photo Detection Efficiency @ 430 nm	PM66	25	26	34	%
		50	28	38	
Dark Count Rate	PM66	25	250	500	kHz/mm ²
		50	250	500	
Crosstalk Probability	PM66	25	16	35	%
		50	16	35	
Afterpulse Probability	PM66	25	1	3	%
		50	1	3	
Gain	PM66	25	0.9	1.7	x 10 ⁶
		50	3.6	7.2	
Terminal Capacitance	PM66	25	2800		pF
		50	3100		
Recovery Time τ	PM66	25	40		ns
		50	70		
Signal Rise Time	PM66	25	1.0		ns
		50			

5. Technical Drawing and Footprint



KETEK GmbH
 Hofer Str. 3
 81737 Munich, Germany
 www.ketek.net
 info@ketek.net
 phone +49 89 673 467 70
 fax +49 89 673 467 77

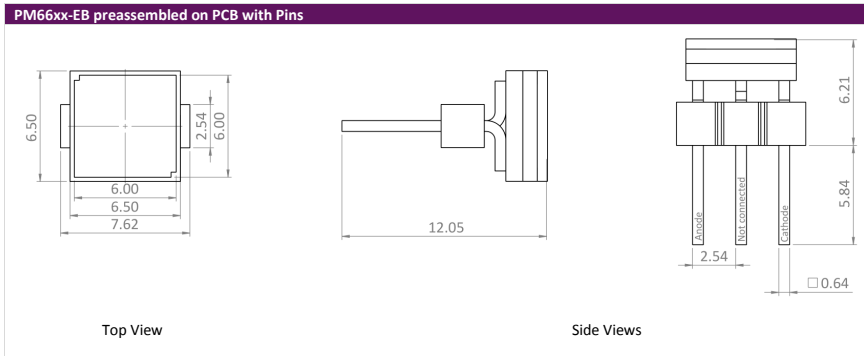




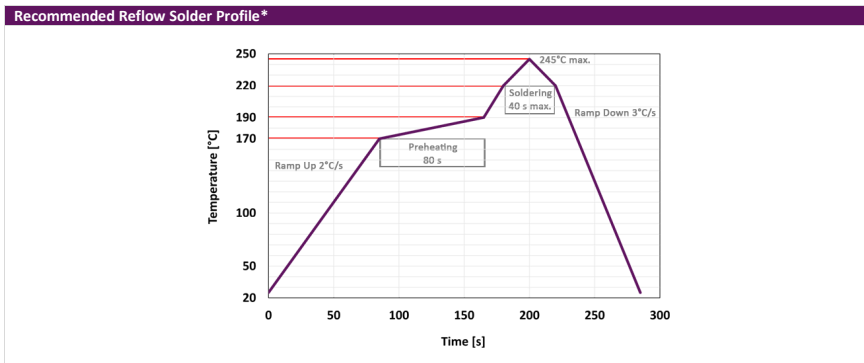
Product Data Sheet
SiPM – Silicon Photomultiplier
PM6625-EB / PM6650-EB



6. Pin Variant



7. Reflow Solder Profile



* Soldering under nitrogen atmosphere is recommended to avoid deterioration of the highly transparent epoxy encapsulation

KETEK GmbH
 Hofer Str. 3
 81737 Munich, Germany
 www.ketek.net
 info@ketek.net
 phone +49 89 673 467 70
 fax +49 89 673 467 77



List of Figures

1	Simple representation of the AEGIS scheme taken from the AEGIS collaboration's website.	4
2	Light yield of pure CsI crystals as a function of temperature read out by a photodiode and a photomultiplier [17].	7
3	Light emission waveform for a pure CsI crystal at 192 K (a) and 85 K (b), measured with a photo-multiplier [17].	7
4	Decay times of the light emission for a pure CsI crystal at different temperatures [17]	8
5	Comparison of the photon detection efficiency of SiPM, PMT and APD [18].	10
6	Temperature dependence of the SiPM dark count rate for different pixel gains [18].	10
7	Schematic representation of the highpass board.	13
8	The pulse-height spectra plotted for slow antiprotons, which arrived in a time window between 2.0-2.6 μ s. The three lines (blue, orange, gray) correspond to the three different SiPMs, respectively.	14
9	Circuit diagram of the amplifier board. The two red circles on the left show the differential entrance.	18
10	Circuit diagram of the amplifier board II.	18
11	Cooling capacity map for the cooling system (PT14) used [21].	19
12	Set-up idea for testing the PMMA light guide pyramid. The light gray pyramid represents the PMMA.	22
13	Transmission curve of a 2 mm thick PMMA sample in air [22].	23
14	Attenuation for ultraviolet wavelengths for the optical fibers used [23].	23
15	Set-up for optical fibers as light guides. The small blue square in the front represents the CsI, the gray lines are the nine 30 cm long fibers guiding the light to the SiPM in the back.	24
16	The set-up used to check if a gap between the scintillators and the silicon photomultipliers would guide a sufficient amount of light to the photomultipliers. The front view shows the gray aluminum block containing the CsI crystals in the middle. The copper wires on the bottom are connected to the CRYOTIGER® I cooling system, responsible for the heat transfer. The two plastic mounts on the left and the right are connecting the whole set-up to the metal rods. In the back the flange with the pins for the electronics' lines can be seen.	26
17	Back view of Fig. 16. In the back the mount (beige) for the SiPMs can be seen.	26
18	Change of temperature in the DN160 cross recorded at different positions. While the scintillators cooled off the SiPMs stayed relatively warm.	27
19	First spectrum recorded with the ADC with a run time of 16.5 hours. The bias voltage applied to the SiPM set the current to 0.56 μ A.	28
20	Comparison of a room temperature plastic scintillator signal (blue) and a cold CsI signal (orange).	29

21	The set-up for the LYSO is similar to Fig. 4.2, instead of three CsI crystals a smaller CsI crystal and a LYSO crystal were used. The flange and rods are not shown in this figure.	31
22	Change of temperature in the DN160 cross recorded at different positions for the new set-up shown in Fig. 21.	32
23	Comparison of ^{22}Na spectra of low temperature CsI and LYSO crystals. A current of $0.6 \mu\text{A}$ was applied to the SiPM facing the LYSO and $3.8 \mu\text{A}$ to the one facing the CsI. These spectra were the results of a 22 hour measurement.	33
24	Comparison of ^{22}Na spectra of low temperature CsI and LYSO crystals. A current of $1.18 \mu\text{A}$ was applied to both SiPMs. These spectra were the results of a 30 minute measurement.	34
25	Comparison of signals of a cold CsI crystal ($-150 \text{ }^\circ\text{C}$) and the signals of the CsI crystal in the same set-up at room temperatures (warm, $20 \text{ }^\circ\text{C}$).	36
26	Comparison of signals of a cold LYSO crystal ($-150 \text{ }^\circ\text{C}$) and the signals of the LYSO crystal in the same set-up at room temperatures (warm, $20 \text{ }^\circ\text{C}$).	36
27	Waveform produced by the LYSO crystal at -150°C while $0.3 \mu\text{A}$ were used to operate the SiPM. The red squares show the start and end points of the fits. In orange is the linear fit for the fall time and in green the exponential fit of the rise time.	37
28	Set-up used for the low temperature behaviour of silicon photomultipliers. The copper block represents the cool tip. The detector is attached to the gray block made out of aluminium in the front. The long hollow cylincer is guiding the light (to avoid reflections at the wall of the DN160 cross) from the LED.	41
29	Dependence of the waveforms on frequency and pulse width. A higher frequency of the pulse produced smaller signals (blue/orange) and a pulse width set too high produced a long and small signal (green). For those waveforms the amplifier board (with an amplification of $V=3$) was used.	42
30	Changes in properties and functionality of a $6\times 6 \text{ mm}^2$ SiPM at different low temperatures. Signals were processed by the highpass board.	43
31	Changes in properties and functionality of a $6\times 6 \text{ mm}^2$ SiPM at different low temperatures. The signals were processed by the amplifier.	44
32	Comparison of vacuum, acrylic plastic, acrylic plastic with grease and acrylic plastic with optical glue in front of the $6\times 6 \text{ mm}^2$ SiPM at 170 K . The signals were processed by the highpass board.	45
33	Changes in properties and functionality of a $4\times 4 \text{ mm}^2$ SiPM at different low temperatures. The signals were processed by the highpass board.	46
34	Changes in properties and functionality of a $3\times 3 \text{ mm}^2$ SiPM at different low temperatures. The signals were processed by the highpass board.	47
35	Set-up for a cryogenic CsI detector.	50
36	Spectra recorded for the three different SiPMs (1 h measuring time, 105 K , $2.5*10^{-7} \text{ mbar}$).	51

37	Energy calibrated spectra recorded for the three different SiPMs (1 h measuring time, 105 K, $2.5 \cdot 10^{-7}$ mbar).	52
38	Spectra recorded at different temperatures for the SiPM in direct contact with the CsI (1 h).	53
39	Spectra recorded at different temperatures for the SiPM with silicon grease (1 h).	53
40	Signals produced by the SiPM (6×6 mm ²) in direct contact with the scintillator.	54
41	Signals produced by the SiPM (6×6 mm ²) connected to the scintillator with optical glue.	55
42	Signals produced by the SiPM (6×6 mm ²) connected to the scintillator with silicon grease.	55
43	Final set-up for the last test at the GRACE line.	58
44	Antiproton shot recorded with one of the detectors at room temperature. No aluminum shield was in front of the scintillators.	59
45	Antiproton shot recorded with one of the detectors at room temperature. With (orange) and without (blue) the aluminium shield in front of the scintillators.	60

References

- [1] G. Dobrychev, P. Nedelec, D. Sillou, G. Gribakin, H. Walters, G. Ferrari, M. Prevedelli, G.M. Tino, M. Doser, C. Canali, C. Carraro, V. Lagomarsino, G. Manuzio, G. Testera, S. Zavatarelli, M. Amoretti, A. Kellerbauer, J. Meier, U. Warring, M.K. Oberthaler, I. Boscolo, F. Castelli, S. Cialdi, L. Formaro, A. Gervasini, G. Giannamarchi, A. Vairo, G. Consolati, A. Dupasquier, F. Quasso, H.H. Stroke, A.S. Belov, S.N. Gninenko, V.A. Matveev, V.M. Byakov, S.V. Stepanov, D.S. Zvezhinskij, M. de Combarieu, P. Forget, P. Pari, L. Cabaret, D. Comparat, G. Bonomi, A. Rotondi, N. Djourelou, M. Jacquay, M. Buchner, G. Trenec, J. Vigue, R.S. Brusa, S. Mariazzi, S. Hogan and F. Merkt, *Proposal for the AEGIS experiment at the CERN Antiproton Decelerator (Antimatter Experiment: Gravity, Interferometry, Spectroscopy)*, CERN-SPSC-2007-017, CERN-SPSC-P-334 (2007).
- [2] W. Bertsche, A. Boston, P.D. Bowe, C.L. Cesar, S. Chapman, M. Charlton, M. Chartier, A. Deutsch, J. Fajans, M.C. Fujiwara, R. Funakoshi, D.Gill, K.Gomberoff, D. Grote, J.S. Hangst, R.S. Hayano, M. Jenkins, L. V. Jørgensen, N. Madsen, D. Miranda, P. Nolan, K. Ochanski, A.Olin, R.D. Page, L.G.C. Posada, F. Robicheaux, E. Sarid, H.H. Telle, J.-L. Vay, J. Wurtele, D.P. van der Werf, and Y. Yamazaki, *The ALPHA Experiment: A Cold Antihydrogen Trap*, AIP Conference Proceedings, **796**, 301-308 (2005).
- [3] M. Hori, H. Aghai-Khozani, A. Sótér, D. Barna, A. Dax, R. Hayano, T. Kobayashi, Y. Murakami, K. Todoroki, H. Yamada, D. Horváth and L. Venturelli, *Buffer-gas cooling of antiprotonic helium to 1.5 to 1.7 K, and antiproton-to-electron mass ratio*, Science **354**, 6312 (2016).
- [4] N. Kuroda, S. Ulmer, D.J. Murtagh, S. Van Gorp, Y. Nagata, M. Diermaier, S. Federmann, M. Leali, C. Malbrunot, V. Mascagna, O. Massiczek, K. Michishio, T. Mizutani, A. Mohri, H. Nagahama, M. Ohtsuka, B. Radics, S. Sakurai, C. Sauerzopf, K. Suzuki, M. Tajima, H.A. Torii, L. Venturelli, B. Wünschek, J. Zmeskal, N. Zurlo, H. Higaki, Y. Kanai, E. Lodi Rizzini, Y. Nagashima, Y. Matsuda, E. Widmann, and Y. Yamazaki, *A source of antihydrogen for in-flight hyperfine spectroscopy*, Nat. Commun. **5**, 3089 (2014).
- [5] Y. Yamazaki, S. Ulmer, *CPT symmetry tests with cold antiprotons and antihydrogen*, Ann. Phys. (Berlin) **525**, No. 7, 493–504 (2013).
- [6] P. Perez and Y. Sacquin, *The GBAR experiment: gravitational behaviour of antihydrogen at rest*, Classical and Quantum Gravity, **29**, 18 (2012).
- [7] M.K. Oberthaler, S. Bernet, E.M. Rasel, J. Schmiedmayer and A. Zeilinger, *Inertial sensing with classical atomic beams*, Phys. Rev. A **54**, 4 (1996).
- [8] The ALPHA Collaboration, A. E. Charman, *Description and first application of a new technique to measure the gravitational mass of antihydrogen*, Nature Communications, **4**, 1785 (2013).

- [9] R. Colella, A. W. Overhauser, S. A. Werner *Observation of Gravitationally Induced Quantum Interference*, Phys. Rev. Lett. **34**, 1472 (1975).
- [10] T. Wagner, S. Schlamminger, J. Gundlach, E. Adelberger, *Torsion-balance tests of the weak equivalence principle*, Classical Quantum Gravity **29**, 184002 (2012).
- [11] H. Dittus, C. Lämmerzahl, *Experimental Tests of the Equivalence Principle and Newton's Law in Space* AIP Conference Proceedings, 758, 10.1063/1.1900510 (2005).
- [12] J. Scherk, *Antigravity: A crazy idea?* Phys. Lett. **88**, 265-267 (1979).
- [13] S. Maury, *The Antiproton Decelerator: AD*, Hyperfine Interactions, **109**, 43–52 (1997)
- [14] CERN Homepage, <https://home.cern/about/accelerators/antiproton-decelerator>.
- [15] crystals.saint-gobain.com, Data Sheet: CsI(Tl), CsI(Na) Cesium Iodide Scintillation Material (2017).
- [16] crystals.saint-gobain.com, Data Sheet: CsI(pure) Cesium Iodide Scintillation Material (2017).
- [17] C. Amsler, D. Grögler, W. Joffrain, D. Lindelöf, M. Marchesotti, P. Niederberger, H. Pruys, C. Regenfus, P. Riedler and A. Rotondi *Temperature dependence of pure CsI: scintillation light yield and decay time*, in Nuclear Instruments and Methods in Physics Research Section A **480**, 494-500 (2002).
- [18] B. Dolgosheina, V. Balagurab, P. Buzhana, M. Danilovb, L. Filatovd, E. Garutic, M. Grolle, A. Ilyina, V. Kantserova, V. Kaplina, A. Karakasha, F. Kayumova, S. Klemind, V. Korbelc, H. Meyerc, R. Mizukb, V. Morgunovb, E. Novikovb, P. Pakhlovb, E. Popovaa, V. Rusinovb, F. Sefkowc, E. Tarkovskymb and I. Tikhomirovb, *Status report on silicon photomultiplier development and its applications*, in Nuclear Instruments and Methods in Physics Research Section A **563**, 368–376 (2006).
- [19] N. Otte, *The Silicon Photomultiplier - A new device for High Energy Physics, Astroparticle Physics, Industrial and Medical Applications*, eConf C0604032 0018 SNIC-2006-0018 (2006).
- [20] N. Pacifico, S. Aghion, J. Alozy, C. Amsler, A. Ariga, T. Ariga, G. Bonomi, P. Bräunig, J. Bremer, R.S. Brusa, L. Cabaret, M. Caccia, M. Campbell, R. Caravita, F. Castelli, G. Cerchiari, K. Chloub, S. Cialdi, D. Comparat, G. Consolati, A. Demetrio, L. Di Noto, M. Doser, A. Dudarev, A. Ereditato, C. Evans, R. Ferragut, J. Fesel, A. Fontana, S. Gerber, M. Giammarchi, A. Gligorova, F. Guatieri, S. Haider, H. Holmestad, T. Huse, E. Jordan, A. Kellerbauer, M. Kimura, D. Krasnický, V. Lagomarsino, P. Lansonneur, G. Lawler, P. Lebrun, X. Llopart, C. Malbrunot, S. Mariazzi, L. Marx, V. Matveev, Z. Mazzotta, G. Nebbia, P. Nedelec, M. Oberthaler, D. Pagano, L. Penasa, V. Petracek, C. Pistillo, F. Prezl, M. Prevedelli, L. Ravelli, L. Resch, O.M. Röhne, A. Rotondi, M. Sacerdoti, H. Sandaker, R. Santoro, P. Scampoli,

- L. Smestad, F. Sorrentino, M. Spacek, J. Storey, I.M. Strojek, G. Testera, I. Tietje, L. Tlustos, E. Widmann, P. Yzombard, S. Zavatarelli, J. Zmeskal and N. Zurlo, *Direct detection of antiprotons with the Timepix3 in a new electrostatic selection beamline*, Nuclear Instruments and Methods in Physics Research Section A, **831**, 12-17 (2016).
- [21] Brooks Automation Polycold system[®], CRYOTIGER[®] I cooling system, Operational Manual (2005).
- [22] C. Joram, *Transmission curves of plexiglass (PMMA) and optical grease*, PH-EP-Tech-Note-2009-003.
- [23] Edmund Optics, 600 μm 0.22 NA UV/VIS Fiber, Datasheet (2017).
- [24] crystals.saint-gobain.com, Data Sheet: LYSO Scintillation Material (2017).
- [25] G. Collazuol, M. G. Bisogni, S. Marcatili, C. Piemonte, and A. Del Guerra *Studies of Silicon Photomultipliers at Cryogenic Temperatures*, Nuclear Instruments and Methods in Physics Research A **628**, 389-392 (2011).